Title

The Tidal-Rotational Shape of the Moon and Evidence for Polar Wander

Journal

Nature, 512(7513)

ISSN

0028-0836 1476-4687

Authors

Garrick-Bethell, Ian
Perera, Viranga
Nimmo, F.
et al.

Publication Date

2014-07-30

DOI

10.1038/nature13639

Peer reviewed

The Tidal-Rotational Shape of the Moon and Evidence for Polar Wander

Authors: Ian Garrick-Bethell[1,2*], Viranga Perera[3], Francis Nimmo[1], and Maria T. Zuber[4]

Affiliations:

[1]Department of Earth and Planetary Sciences, University of California, Santa Cruz, 1156 High Street, Santa Cruz, CA 95064.

[2]School of Space Research, Kyung Hee University, 1 Seocheon-dong, Giheung-gu, Yongin-si, Gyeonggi-do 446-701, Korea

[3]School of Earth and Space Exploration, Arizona State University, PO Box 871404, Tempe, AZ 85287-1404.

[4]Department of Earth, Atmospheric and Planetary Sciences, Massachusetts Institute of Technology, 77 Massachusetts Avenue, Cambridge, MA 02139.

*Correspondence to: igarrick@ucsc.edu, (401) 301-5237.

Summary paragraph: The origin of the Moon's large-scale topography is important for understanding lunar geology[1], lunar orbital evolution[2], and the Moon's orientation in the sky[3]. Previous hypotheses for its origin have included late accretion events[4], large impacts[5], tidal effects[6], and convection processes[7]. However, testing these hypotheses and quantifying the Moon's topography is complicated by the large basins that have formed since the crust crystallized. Here we estimate the low-order lunar topography and gravity spherical harmonics outside these basins and show that the bulk of the degree-2 topography is consistent with a crust-building process controlled by early tidal heating throughout the Moon. The remainder of the degree-2 topography is consistent with a frozen tidal-rotational bulge that formed later, at a semi-major axis of ≈32 Earth radii. The probability of the degree-2 shape having these two separate tidal characteristics by chance is less than 1%. We also infer that internal density contrasts eventually reoriented the Moon's polar axis 36 ± 4°, to the present configuration we observe today. Together, these results link the geology of the near and far sides, and resolve long-standing questions about the Moon's low-order shape, gravity, and history of polar wander.

Main Text

The theory of equilibrium figures of rotating fluid bodies is a classic problem in geophysics, and it has been helpful in understanding the shapes of the Sun and planets. However, the origin for the Moon's shape has remained an open problem in the last century[2,6,8-10], and the body's deviations from any simple tidal-rotational (spherical harmonic degree-2) figure are large[11]. This difficulty is surprising given the Moon's presumably simple early thermal history: born hot and quickly cooled, one might expect the Moon to be described by a simple figure of equilibrium.

Researchers have traditionally suggested that the Moon's degree-2 spherical harmonic gravity coefficients, which have been used as proxies for the degree-2 shape, are especially large when compared to higher degree coefficients[9,12]. Figure 1 shows a power law or "Kaula's rule" fit to degrees n = 3 to 50 for the Moon's gravity[13] and topography data[14]. The power at degree 2 is 4.5 times and 2.6 times the power expected from extrapolating the best-fit power law, for gravity and topography, respectively, supporting the idea that the degree-2 coefficients are unique. Indeed, the fraction of excess power for topography is greater than the excesses for Venus, Earth, and Mars (SI). Authors have tried to interpret the Moon's strong degree-2 power as a frozen tidal-rotational state inherited from when the Moon was closer to the Earth, known as the fossil bulge hypothesis[6]. An open problem, however, has been that the ratio of the $C_{2,0}$ and $C_{2,2}$ spherical harmonic coefficients is different from the expected value by a factor of 2.6 (refs. 2,10).

Adding to the fossil bulge idea and motivated by tidal processes in Europa's ice shell[15], Garrick-Bethell et al.[16] inferred that the farside highlands crust has a degree-2 shape explainable by tidal heating during the magma ocean epoch. However, they left open the rest of the Moon's shape, the Moon's orientation history, and the details of gravity and topography when they are examined together. In particular, they did not reconcile their results with the classic fossil bulge hypothesis[10], or explain its anomalous $C_{2,0}/C_{2,2}$ ratio. To address these problems and create a unified explanation for the Moon's degree-2 shape and orientation, we will consider two effects: the Moon's largest basins, and the reference frame in which we analyze lunar topography.

The South Pole-Aitken basin (SPA) is the largest[17], deepest[1], and oldest lunar basin[5], and its degree-2 power affects our interpretation of the primordial degree-2 shape. In addition to SPA, we focus on the 12 largest basins that produce obvious local anomalies in topography, crustal thickness, or gravity (in all, 22% of the surface, Fig. 2a-c). To determine the Moon's degree-2 shape without these basins, we fit spherical harmonics of degrees n = 0 to 5 to data outside their boundaries. Figures 2d and 2f show the Moon's topography and appearance after rotation to the reference frame where the only non-zero degree-2 terms are $C_{2,0}$ and $C_{2,2}$ (with $C_{2,0} < 0$), hereafter the "principal frame." If the Moon's outer figure, as opposed to its internal density distribution, once controlled the lunar moments of inertia (revisited later), this would be the reference frame that once faced Earth. This frame's largest principal axis is at (-6 ± 4°, 30 ± 1° E), its polar axis is at (54 ± 5°, 309 ± 6°), and its intermediate axis is at (-35.1 ± 5°, 296.4 ± 4°) (Figs. 2a-c).

Without the largest basins, the Moon's topography power spectrum displays substantially less variance at low degrees. Performing a power-law fit for n = 3 to 50 using the new power at degrees 3, 4 and 5 (Fig. 1, dashed red line), we find the degree-3 and degree-4 power is much closer to the predictions from Kaula's rule. However, the degree-2 power remains in excess by a factor of 2.8. The Moon's strong degree-2 power, even without its large basins, implies that purely local explanations for the degree-2 character of the farside, such as a late-accreting second moon[4], are less plausible.

To address the origin of the Moon's primordial degree-2 shape, we must also consider the degee-2 gravity potential of the Moon (Fig. 2b). If we again fit degree-2 coefficients outside the basins, we find that gravity's largest principal axis shifts only 5 ± 2°, from (0°, 180° E) to (-5 ± 2°, 182 ± 1° E), and its polar axis only 5 ± 2° to (85 ± 2°, 203 ± 35°) (SI Table S7). In addition, the degree-2 gravity power decreases by a small amount, 12% (Fig. 1, blue dot). The weak effect of basins on the degree-2 gravity potential is partly due to SPA's nearly-compensated state[18], and SPA's large contribution (45%) to the area removed.

The gravity and topography principal frame calculations above reveal a previously unappreciated but critical problem in understanding the lunar shape: while both gravity and topography have

anomalously high degree-2 power, the principal topography and gravity reference frames do not align presently (*i.e.* using global data), and nor do they when using degree-2 harmonics fit outside the largest basins. Using global data, the largest gravity and topography principal axes are separated by 34°, and using data outside large basins, the largest principal axes are separated by 30° ± 5°. Therefore, other non-basin events distorted the Moon from any single, simple equilibrium figure in either gravity or topography, making it ambiguous which data set represents the primordial frame where any tidal-rotational effects were acquired.

However, a simple argument suggests that topography's principal frame formed first. Degree-2, tidally-produced crustal thickness variations[16], if they exist, must have developed early when the lithosphere was weak enough to permit significant tidal flexing, and will therefore be isostatically compensated (with a relatively small gravity signature). Furthermore, any uncompensated fossil component of shape, if it exists, must have frozen-in after the lithosphere cooled and strengthened, and degree-2 crustal thickness growth largely ceased. Therefore, as long as the crustal thickness variations produced degree-2 topography that dominated any subsequent fossil topography, and the principal axes remained mostly fixed while forming, topography's principal frame will be the Moon's first-established Earth-oriented principal frame. Below we will demonstrate that topography components from both crustal-thickening (compensated) and fossil-bulge (uncompensated) processes likely exist in topography's principal frame, with the crustal component being larger, and that each topography component has the $C_{2,0}/C_{2,2}$ ratio expected from each unique process.

To assess the nature of the degree-2 topography in the primordial, basin-removed principal topography frame, we examine the associated gravity harmonics in the same frame (Fig. 2e). In this frame, we use a joint analysis of gravity and topography to find that neither completely compensated nor completely uncompensated topography can alone explain the $C_{2,0}$ and $C_{2,2}$ gravity coefficients (SI Section S4). However, in Table 1 we show that a linear combination of compensated and uncompensated topography is consistent with gravity and topography observations; the topography is effectively ≈80% compensated (shown graphically in SI Fig. S9).

Table 1. Solution for the combination of compensated and uncompensated topography to match the $C_{2,0}$ and $C_{2,2}$ gravity and topography harmonics shown in Fig. 2d and 2e. Compensated and uncompensated topography are associated with crustal thickness variations and a frozen fossil bulge, respectively. The solution assumes a crustal density 2550 kg/m^3, mantle density 3200 kg/m^3, mean lunar density 3340 kg/m^3, and a mean crustal thickness of 40 km[19]. $C_{2,0}$ values do not sum to -0.65 km due to rounding.

	Compensated topography ($\pm$ 1σ)	Uncompensated topography ($\pm$ 1σ)
$C_{2,0}$	-0.53 ± 0.07 km	-0.11 ± 0.04 km
$C_{2,2}$	0.40 ± 0.06 km	0.11 ± 0.03 km
$C_{2,0}/C_{2,2}$	-1.3 ± 0.2	-1.0 ± 0.3

Having established that both fossil (uncompensated) and crustal thickness (compensated) topography components are required, we can examine their coefficient ratios to test their origins. The ratio of $C_{2,0}/C_{2,2}$ for normalized gravity and topography coefficients is -0.96 (≈-1.0) for frozen tidal-rotational fossil bulges in low-eccentricity synchronous orbits (and normalized polar moment of inertia = 0.4)[10,12,20]. The classic problem has been that the observed present-frame ratio is very different from -1.0: -2.6 for global gravity[2,10] (Fig. 2b) and -6.1 for global topography (Fig. 2a). However, we must now also consider the expected topography ratio for tidally-controlled crustal thickness variations[16]. Unlike the case for fossil topography, this ratio is variable, depending on the amount of tidal dissipation. While dissipation depends on a number of parameters that are difficult to estimate, such as lower crustal viscosity, we find that for 114 model calculations spanning a variety of conditions, $C_{2,0}/C_{2,2}$ approaches -1.1 to -1.3 as the mean global tidal heat flux increases above ≈50 mW/m^2 (Fig. 3).

From Table 1, we see the ratio $C_{2,0}/C_{2,2}$ for compensated topography in topography's principal frame is -1.3 ± 0.2, and for uncompensated topography, the ratio is -1.0 ± 0.3. These values are consistent with the ratios predicted for a crust sculpted by tidal heating, and a frozen fossil-bulge, respectively. A similar spherical harmonic coefficient fit to a model of crustal thickness[19], with large basins removed, yields $C_{2,0}/C_{2,2}$ = -1.1 ± 0.2 (SI Fig S10), in good agreement with the compensated topography ratio. The observed topography $C_{2,0}/C_{2,2}$ ratios are robust (compared to their uncertainties) to the inclusion or exclusion of different basins, as well as increases in the size of SPA up to 50% (30% for other basins), and changes in the maximum fit degree (SI Table S4). If we had not removed the effects of large basins, the solution for compensated and

uncompensated topography in the global-topography principal frame yields $C_{2,0}/C_{2,2}$ values of -2.0 and -6.1, respectively (SI Table S10).

To assess the likelihood that the unique $C_{2,0}/C_{2,2}$ ratios arise by chance, we performed Monte Carlo simulations with topography and gravity with the same statistical properties as the observed data. This topography and gravity could arise from any source, including early mantle convection processes, or the process that produced the Moon's center-of-mass/center-of-figure offset. We find that the probabilities of the compensated and uncompensated topography $C_{2,0}/C_{2,2}$ ratios randomly falling between -1.1 to -1.3, and -0.9 to -1.1 (ranges taken to represent the predicted values for each mechanism), are 8% and 5%, respectively (SI Section 9, Figs. S12 & S13). The joint probability is only 0.3%, suggesting the degree-2 shape is tidally produced.

In the principal topography frame, we also obtain gravity terms $S_{2,1}$, $C_{2,1}$, and $S_{2,2}$, which constitute 59% of the basin-removed degree-2 gravity power (Fig. 2e). Since these terms are associated with zero topography, they arise from subsurface density anomalies that must have developed after a rigid lithosphere formed. Dynamically-produced hemisphere-scale density changes have been proposed[21-23] , and they would likely have degree-2 power that could have affected the Moon's degree-2 tidal signatures. We can estimate the probability that the Moon's tidal characteristics would survive such an event. For example, starting with just the $C_{2,0}$ and $C_{2,2}$ gravity and topography values for the basin-removed Moon, a randomly placed hemisphere-sized gravity anomaly that yields the same total degree-2 gravity power as the basin-removed Moon, permits survival (<30% alteration) of the compensated topography $C_{2,0}/C_{2,2}$ ratio 92% of the time, and the uncompensated ratio 37% of the time (SI Section S10). This simple model demonstrates that if the Moon's unique tidal signatures form (which is seldom by chance, above), their recovery is quite plausible despite subsequent internal gravity changes. This is largely because the $C_{2,0}/C_{2,2}$ ratios are dependent on topography, not gravity alone.

Our tidal calculations indicate that above semi-major axis $a \approx 25$ Earth radii (R_E), no realistic models can produce significant tidal heating, and below $a \approx 10R_E$, the orbital evolution timescales (<1 My) are too short to have built a significant amount of crust. The uncompensated $C_{2,0}$ and $C_{2,2}$ values imply fossil freeze-in at $a \approx 32R_E$, or $30R_E$ allowing for 18% relaxation after

4 billion years[24]. This freeze-in location is larger than $25R_E$ (above), and therefore consistent with the requirement that the lithosphere forms after the crust-building epoch. The location is also consistent with freeze-in before the Cassini state transition (≈30-34 R_E)[25], which would have affected the lunar shape. Nominally, it takes roughly 200-300 My for the Moon to evolve to $32R_E$ after accretion[26]. This lithosphere development timescale is consistent with estimates of 100-200 My for complete magma ocean crystallization, based on radioisotope studies and thermal-modeling[27-29]. By combining timescales such as these, and our inferred fossil formation position at $a \approx 32R_E$, the orbital evolution and tidal properties of the early Earth-Moon system can be further constrained.

Finally, we find the principal topography frame places the Moon's paleopole in northern Oceanus Procellarum (54 ± 5°, 309 ± 6°), and about 30° from the center of the thorium-rich Procellarum KREEP Terrane (SI Fig. S14). This paleopole location may be testable by using the poles of magnetized portions of the crust[30]. Eventually, the additional gravity in $C_{2,1}$, $S_{2,1}$, and $S_{2,2}$, plus the basins we have removed, changed the lunar moments of inertia, and reoriented the Moon to the present frame we see today. While the details and timing of these later processes are not yet fully understood, a self-consistent origin of the primordial degree-2 shape helps provide a framework for understanding the many subsequent events in lunar evolution.

References:

1 Zuber, M. T., Smith, D. E., Lemoine, F. G. & Neumann, G. A. The Shape and Internal Structure of the Moon from the Clementine Mission. *Science* **266**, 1839-1843 (1994).

2 Jeffreys, H. On the figures of the Earth and Moon. *Geophys. J. Int.* **4**, 1-13 (1937).

3 Melosh, H. J. Large impact craters and the moon's orientation. *Earth and Planet. Sci. Lett.* **26**, 353-360 (1975).

4 Jutzi, M. & Asphaug, E. Forming the lunar farside highlands by accretion of a companion moon. *Nature* **476**, 69-72 (2011).

5 Wilhelms, D. E. *The geologic history of the Moon, USGS Prof. Paper 1348*. (US Govt. Printing Office, 1987).

6 Sedgwick, W. F. On the figure of the Moon. *Messenger Math.* **27**, 171-173 (1898).

7 Loper, D. E. & Werner, C. L. On lunar asymmetries 1. Tilted convection and crustal asymmetry. *J. Geophy. Res.* **107**, doi: 10.1029/2001JE001442 (2002).

8 Urey, H. C., Elsasser, W. M. & Rochester, M. G. Note on the internal structure of the Moon. *Ap. J.* **129**, 842-848 (1959).

9 Lambeck, K. & Pullan, S. The lunar fossil bulge hypothesis revisited. *Phys. Earth Planet. Inter.* **22**, 29-35 (1980).

10 Stevenson, D. J. Origin and implications of the degree two lunar gravity field. *Proc. Lunar Sci. Conf. 32nd*, 1175 (2001).
11 Smith, D. E., Zuber, M. T., Neumann, G. A. & Lemoine, F. G. Topography of the Moon from the Clementine LIDAR. *J. Geophy. Res.* **102**, 1591-1611 (1997).
12 Williams, J. G., Boggs, D. H., Yoder, C. F., Ratcliff, J. T. & Dickey, J. O. Lunar rotational dissipation in solid body and molten core. *J. Geophy. Res.* **106**, 27933-27968 (2001).
13 Zuber, M. T. *et al.* Gravity field of the Moon from the gravity recovery and interior laboratory (GRAIL) mission. *Science* **339**, 668-671 (2013).
14 Smith, D. E. *et al.* Initial observations from the Lunar Orbiter Laser Altimeter (LOLA). *Geophys. Res. Lett.* **37**, CiteID L18204 (2010).
15 Ojakangas, G. W. & Stevenson, D. J. Thermal state of an ice shell on Europa. *Icarus* **81**, 220-241 (1989).
16 Garrick-Bethell, I., Nimmo, F. & Wieczorek, M. A. Structure and formation of the lunar farside highlands. *Science* **330**, 949-951 (2010).
17 Garrick-Bethell, I. & Zuber, M. T. Elliptical structure of the lunar South Pole-Aitken basin. *Icarus* **204**, 399-408 (2009).
18 Namiki, N. *et al.* Farside Gravity Field of the Moon from Four-Way Doppler Measurements of SELENE (Kaguya). *Science* **323**, 900-905 (2009).
19 Wieczorek, M. A. *et al.* The crust of the Moon as seen by GRAIL. *Science* **339**, 671-675 (2013).
20 Garrick-Bethell, I., Wisdom, J. & Zuber, M. T. Evidence for a past high eccentricity lunar orbit. *Science* **313**, 652-655 (2006).
21 Zhong, S., Parmentier, E. M. & Zuber, M. T. A dynamic origin for the global asymmetry of lunar mare basalts. *Earth and Planet. Sci. Lett.* **177**, 131-140 (2000).
22 Laneuville, M., Wieczorek, M. A., Breuer, D. & Tosi, N. Asymmetric thermal evolution of the Moon. *J. Geophy. Res.* **118**, 1435-1452 (2013).
23 Melosh, H. J. Mascons and the moon's orientation. *Earth and Planetary Science Letters* **25**, 322-326 (1975).
24 Zhong, S. & Zuber, M. T. Long-wavelength topographic relaxation for self-gravitating planets and implications for the time-dependent compensation of surface topography. *J. Geophy. Res.* **105**, 4153-4164 (2000).
25 Siegler, M. A., Bills, B. G. & Paige, D. A. Effects of orbital evolution on lunar ice stability. *J. Geophy. Res.* **116**, E03010 (2011).
26 Dwyer, C. A., Stevenson, D. J. & Nimmo, F. A long-lived lunar dynamo driven by continuous mechanical stirring. *Nature* **470**, 212-214 (2011).
27 Solomon, S. C. & Longhi, J. Magma oceanography: 1. Thermal evolution. *Proc. Lunar Sci. Conf. 8th*, 583-599 (1977).
28 Borg, L. E., Connelly, J. N., Boyet, M. & Carlson, R. W. Chronological evidence that the Moon is either young or did not have a global magma ocean. *Nature* **477**, 70-72 (2011).
29 Meyer, J., Elkins, L. T. & Wisdom, J. Coupled thermal–orbital evolution of the early Moon. *Icarus* **208**, 1-10 (2010).
30 Runcorn, S. K. Lunar magnetism, polar displacements and primeval satellites in the Earth-Moon system. *Nature* **304**, 589-596 (1983).

Acknowledgements:

This work was supported by the BK21 plus program through the National Research Foundation (NRF), funded by the Ministry of Education of Korea. Conversations with E. Mazarico are appreciated. We acknowledge the GRAIL and LRO teams for the gravity and topography data used in the analysis.

Author contributions:

IG-B and MTZ planned the research. VP performed the power law calculations and helped develop the spherical harmonic fitting procedures. FN performed the tidal heating calculations. IG-B performed the remainder of the research and wrote the paper. Reprints and permissions information is available at www.nature.com/reprints. The authors declare no competing financial interests. Correspondence and requests for materials should be addressed to igarrick@ucsc.edu.

Methods Summary:

Spherical harmonic coefficients were fit outside large basins with a least squares algorithm. Monte Carlo methods were used to estimate uncertainties that arise from the non-orthogonal nature of spherical harmonics calculated on a partial sphere. The maximum spherical harmonic degree of the fit was determined by the largest degree that minimized the total error, before the solution became unstable due to the size of the unfit area inside the South Pole-Aitken basin. The equations for the amounts of degree-2 compensated and uncompensated topography are based on the work of ref. 38. The probability of finding the characteristic compensated and uncompensated topography $C_{2,0}/C_{2,2}$ ratios by chance is based on the statistics of the ratios of the Moon's higher degree topography harmonics. The tidal heating calculations are based on the methods discussed in ref. 16. See Supplementary Information for more details.

Figure captions:

Fig. 1. Lunar topography and gravity power, with best-fit power laws for degrees n = 3 to 50. The blue dots show the power using data outside of large basins ($\pm 1\sigma$). The blue dot at degree-1 for gravity is due to a small displacement of the lunar center of mass when the basins are removed.

Fig. 2. The topography, gravity, and appearance of the Moon, with black lines illustrating basins removed in the analysis. (**A**) Lunar topography. Black circles, triangles, and squares are the primordial minimum, intermediate, and maximum principal moment of inertia axes, respectively, respectively (also used in parts B and C, Table S7). (**B**) Expansion of degree 2 to 360 lunar gravity potential coefficients (multiply by 2.823×10^6 m^2 s^{-2} to obtain surface potential). (**C**) Lunar 750-nm spectral reflectance, with data above 75° latitude blacked out. (**D**) Part A after rotation to the topography principal frame, using rotation angles calculated from data outside of large basins. (**E**) Part B after rotating to the topography principal frame, as in part D. (**F**) Part C after rotation to the principal topography frame, as in part D.

Fig. 3. The ratio $C_{2,0}/C_{2,2}$ for crustal thickness (or compensated topography), as a function of global mean tidal heat flux, for 114 model cases considered (Table S13). The observed ratio of -1.3 ± 0.2 (1σ, dashed lines) for compensated topography outside of large basins is illustrated (Table 1). Inset: Model crustal thickness map with $C_{2,0}/C_{2,2} = -1.26$ (SI Section S8).

Supplementary Information:

Methods

Figures S1-S14

Tables S1-S13

References (31-53)

Fig. 1

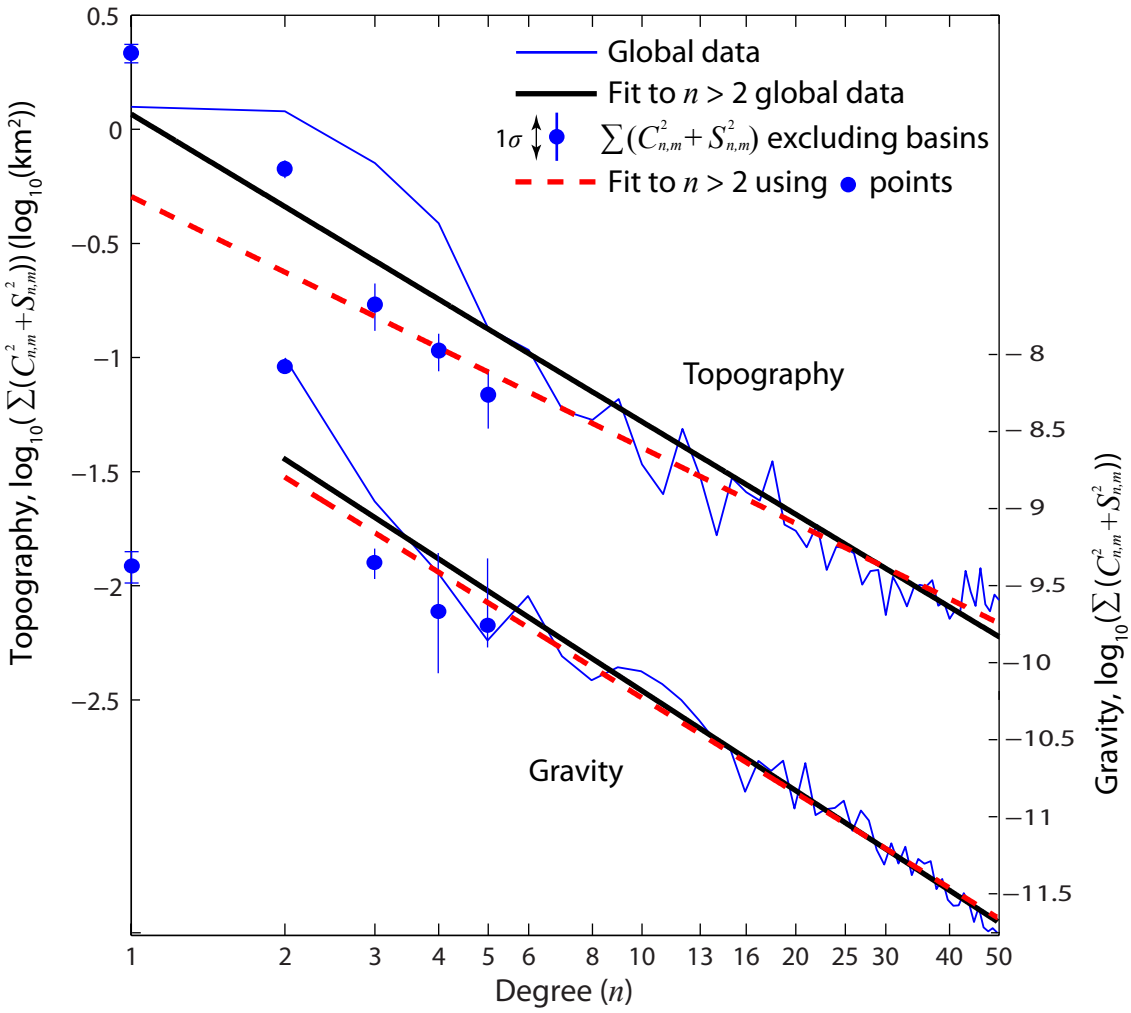
Global data
Fit to $n > 2$ global data
1σ $\sum(C_{n,m}^2 + S_{n,m}^2)$ excluding basins
Fit to $n > 2$ using points
Topography
Gravity
Topography, $\log_{10}(\sum(C_{n,m}^2 + S_{n,m}^2))$ $(\log_{10}(\text{km}^2))$
Gravity, $\log_{10}(\sum(C_{n,m}^2 + S_{n,m}^2))$
Degree (n)
0.5
0
−0.5
−1
−1.5
−2
−2.5
−8
−8.5
−9
−9.5
−10
−10.5
−11
−11.5
1
2
3
4
5
6
8
10
13
16
20
25
30
40
50

Fig. 2

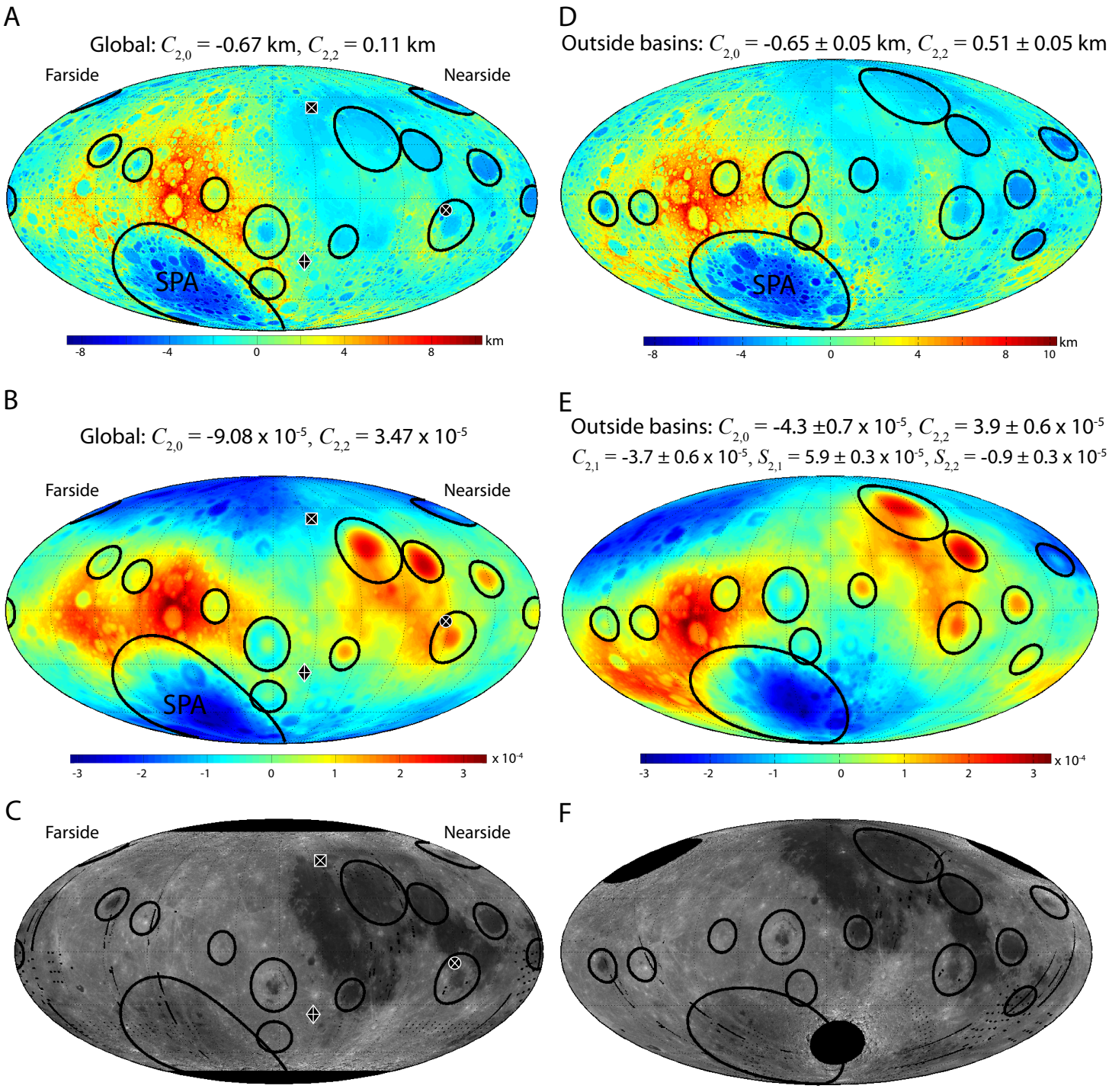
A
Global: $C_{2,0}$ = -0.67 km, $C_{2,2}$ = 0.11 km
Farside
Nearside
SPA
-8
-4
0
4
8
km
D
Outside basins: $C_{2,0}$ = -0.65 ± 0.05 km, $C_{2,2}$ = 0.51 ± 0.05 km
SPA
-8
-4
0
4
8
10
km
B
Global: $C_{2,0}$ = -9.08 x 10^{-5}, $C_{2,2}$ = 3.47 x 10^{-5}
Farside
Nearside
SPA
-3
-2
-1
0
1
2
3
x 10^{-4}
E
Outside basins: $C_{2,0}$ = -4.3 ±0.7 x 10^{-5}, $C_{2,2}$ = 3.9 ± 0.6 x 10^{-5}
$C_{2,1}$ = -3.7 ± 0.6 x 10^{-5}, $S_{2,1}$ = 5.9 ± 0.3 x 10^{-5}, $S_{2,2}$ = -0.9 ± 0.3 x 10^{-5}
-3
-2
-1
0
1
2
3
x 10^{-4}
C
Farside
Nearside
F

Fig. 3

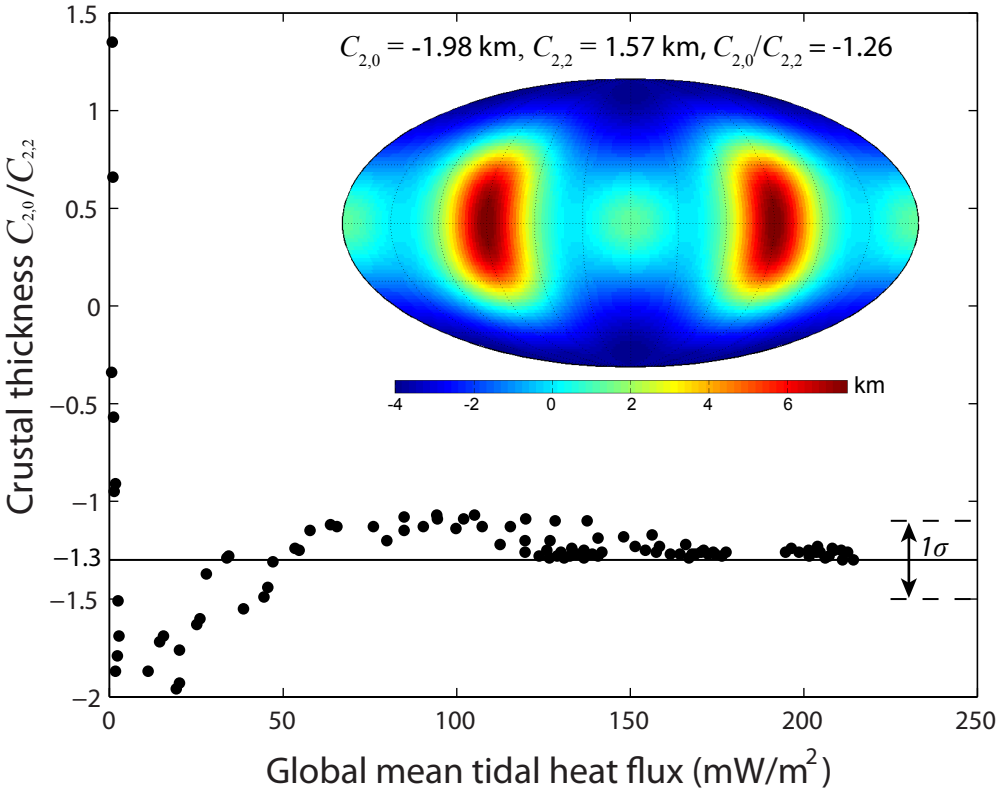
$C_{2,0}$ = -1.98 km, $C_{2,2}$ = 1.57 km, $C_{2,0}/C_{2,2}$ = -1.26
km
-4
-2
0
2
4
6
Crustal thickness $C_{2,0}/C_{2,2}$
1.5
1
0.5
0
−0.5
−1
−1.3
−1.5
−2
1σ
0
50
100
150
200
250
Global mean tidal heat flux (mW/m^2)

Supplementary Information for

The Tidal-Rotational Shape of the Moon and Evidence for Polar Wander

Ian Garrick-Bethell, Viranga Perera, Francis Nimmo, and Maria T. Zuber

correspondence to: igarrick@ucsc.edu

This PDF file includes:

S1. Topography and gravity power spectra methods

S1.1 - Background and methods

A body's gravitational potential U can be represented by a sum of spherical harmonic functions,

$$U = \frac{GM}{r}\sum_{n=0}^{\infty}\sum_{m=0}^{n}\left(\frac{R}{r}\right)^{n} P_{n,m}\left(\sin\varphi\right) \times \left[C_{n,m}\cos m\theta + S_{n,m}\sin m\theta\right] \quad , \tag{S1}$$

and its topography t can be represented similarly,

$$t = R + \sum_{n=1}^{\infty}\sum_{m=0}^{n} P_{n,m}\left(\sin\varphi\right) \times \left[C_{n,m}\cos m\theta + S_{n,m}\sin m\theta\right] \quad , \tag{S2}$$

where R is the planet's reference radius, r is the observation radius, G is the gravitational constant, M is the planet's mass, $P_{n,m}$ are associated Legendre polynomials of degree n and order m, $C_{n,m}$ and $S_{n,m}$ are the normalized spherical harmonic coefficients, φ is latitude, and θ is longitude. The harmonics are normalized by equation 3 of ref. 31. We define the power W by (ref. 31),

$$W(n) = \sum_{m=0}^{n} C_{n,m}^2 + S_{n,m}^2 \quad . \tag{S3}$$

The power spectra of planetary topography and gravity can often be approximated by a power law, known as Kaula's rule[32],

$$\log_{10} W = a\log_{10}(n) + b \quad . \tag{S4}$$

Equation S4 was used to calculate the best-fit lines shown in Fig. 1 in the main text.

S1.2 - Uniqueness of the Moon's degree-2 power

To assess the uniqueness of the Moon's degree-2 power relative to other bodies, we can compare the lunar power spectrum to gravity and topography spectra of Venus, Mars, and the Earth (for an earlier analysis of this problem see ref. 33). Before we do so, we remove the rotational hydrostatic component from the Earth and Mars from their $C_{2,0}$ terms. For the Moon and Venus, the rotational deformation is small enough to be ignored.

To estimate the hydrostatic flattening we first use the Darwin-Radau relation to estimate the fluid deformation Love number h_2 from the polar moment of inertia C,

$$\frac{C}{MR^2} = \frac{2}{3}\left[1 - \frac{2}{5}\left(\frac{5}{h_2} - 1\right)^{1/2}\right] \quad . \tag{S5}$$

For Mars, we assumed $C = 0.365MR^2$ (ref. 34) and for the Earth $C = 0.3307MR^2$ (ref. 35). The hydrostatic ellipticity is obtained from

$$\frac{\delta - \epsilon}{R} = \frac{1}{2}\frac{R^3\omega^2}{GM}h_2 \quad , \tag{S6}$$

where δ is the equatorial radius, ϵ is the polar radius, and ω is the planetary rotation rate. The ellipticity was then converted to the equivalent $C_{2,0}$ value, which was subtracted from the observed topography. For gravity, we subtracted the hydrostatic gravity coefficient $C_{2,0}$ using

$$C_{2,0} = \frac{C - A}{MR^2} = \frac{1}{3}\frac{R^3\omega^2}{GM}k_2 \quad , \tag{S7}$$

where $k_2 = h_2 - 1$, and A is the minimum principal moment of inertia.

Figure S1 shows the best-fit power spectra (eq. S4) for degrees 3 to 50 for Venus, Earth, Mars, and the Moon with and without large basins. Table S1 gives the best-fit power law coefficients a and b. To calculate the best-fit power law for lunar topography and gravity without large basins, we substituted the global degree 3 to 5 coefficients with the values shown in Tables S5 and S6. The methods used to calculate these coefficients and their uncertainties are discussed in Section S2.

Table S2 shows the ratio of the observed degree-2 power and the power at degree-2 from extrapolating the best-fit power law for Venus, Earth, Mars, and the Moon (with and without large basins). Using global data, the Moon's degree-2 topography power is 2.6 times higher than its best-fit power at degree 2. Excluding large basins, the degree-2 topography power is 2.8 times higher than its best-fit power extrapolated to degree 2, which is still higher than the any of the other bodies shown. This implies that the Moon's degree-2 topography power can still be considered "anomalous" even when large basins are removed.

Interestingly, the Earth, Mars and the Moon all show excess degree-2 gravity power, with observed/extrapolated power ratios of 4.4, 6.4, and 4.5, respectively (Table S2). Using a lunar gravity power law excluding large basins, the degree-2 power is in excess by a factor of 5.2. On Mars, the excess degree-2 power can be explained by Tharsis. To demonstrate this, we removed Tharsis according to the methods of Zuber and Smith (1997)[36]. We find that the degree-2 observed/extrapolated power ratio for Mars is reduced to 0.23 and 0.48 for topography and gravity, respectively, when Tharsis is removed. For the Earth, there are several theories for the origin of the low degree gravity power (e.g. ref. 33), including mantle density anomalies.

S2. Spherical harmonic coefficient estimation methods

S2.1 - Methods

The Moon's large basins are local features that have spherical harmonic power at all degrees, and we seek an estimate of the Moon's low-degree coefficients without their contributions. To estimate topography and gravity harmonics outside of these basins, we performed least-squares regressions to data outside of their boundaries (defined in Section S2.2). The least squares

method was tested on global data sets and reproduced the input coefficients with errors < 0.01%. Uncertainties associated with the non-orthogonal nature of spherical harmonics on a partial sphere are discussed in Section S2.6.

Using the estimated degree-2 harmonics, we calculate the "principal" reference frame that brings the minimum moment of inertia into the Earth-Moon line, and the maximum moment of inertia into the polar axis (for topography, the assumption is that the topography influences the moment of inertia). This reference frame has only $C_{2,0}$ and $C_{2,2}$ terms (with $C_{2,0}$ negative), and this frame is calculated by diagonalizing the following matrix, using unnormalized coefficients (e.g. ref. 37):

$$\begin{bmatrix} \frac{1}{3}C_{2,0} - 2C_{2,2} & -2S_{2,2} & -C_{2,1} \\ -2S_{2,2} & \frac{1}{3}C_{2,0} + 2C_{2,2} & -S_{2,1} \\ -C_{2,1} & -S_{2,1} & -\frac{2}{3}C_{2,0} \end{bmatrix} . \quad \text{(S8)}$$

The resulting eigenvectors were then converted into three sequential rotations required to bring the present Earth-facing reference frame into the new principal frame. As shown in Fig. S2, the rotation angles are all referenced to a point on the farside anti-Earth point (0° N, 180° E), and performed in the following order:

1) Shift in longitude θ (positive values shift data eastward),

2) Shift in latitude φ (positive values shift farside data south),

3) Finally, rotation about the largest principal axis, passing through (0°, 180°), λ (positive values clockwise when viewed from the farside).

S2.2 - Choice of basins and their boundaries

For the South Pole-Aitken basin (SPA), we used the "outer" topography SPA boundaries defined by Garrick-Bethell and Zuber (2009)[17], except we use the "inner" topography center, which is further north by 1.8°. These boundaries are centered at (-53.2°, 191° E), and have a semi-major axis of 1200 km, semi-minor axis of 1030 km, and a tilt angle of -18.8° (positive is a rotation clockwise when viewing the farside).

We also identified the next 12 largest basins with clearly defined signatures in topography, gravity, or crustal thickness. While several lunar basins or purported basins are larger than those included in our analysis, they have very weak or poorly defined topography, gravity, or crustal thickness signatures. For example, Mare Tranquilitatis and Mare Nubium were not included in our study. Figure S3 shows maps of topography, crustal thickness, and gravity, to illustrate all basin boundaries, and Table S3 lists the basin names and properties. In some cases, such as Orientale, there are positive crustal thickness anomalies included in the basin boundaries. In other cases, such as Imbrium and Serenitatis, the basins have minimal topography expressions, but strong positive gravity anomalies (mascons).

S2.3 - Effect of maximum fit degree

Because spherical harmonics of different degrees are not orthogonal when fit over a partial sphere, the degree-2 coefficients we seek will change as a function of the maximum fit degree. As the maximum fit degree increases, the total error of the solution decreases, but above degree 5 the "hole" created by SPA becomes apparent in the best-fit solution. This strong distortion of the solution results from no constraints on the solution in the SPA region (Fig. S4). The distortion appears at degree 6 because the size of SPA's boundary is approximately degree 5 to 6.

For gravity and topography, the best-fit coefficients and rotation angles θ, φ, and λ are generally similar for maximum fit degrees less than 6 (illustrated in Fig. S5). However, at degree 6, $C_{2,0}$ for topography starts to decrease monotonically, and the angles θ, φ, and λ also exhibit abrupt changes. Most significantly, the ratios $C_{2,0}/C_{2,2}$ for compensated and uncompensated topography are stable up to degree 5, but start to change rapidly at degree 6. This is not surprising given the distortion visible for degrees higher than 5 in Fig. S4.

The topography power spectra are relatively consistent for maximum fit degrees up to 5. However, the degree 2 to 5 power abruptly increases when the maximum fit degree is 6 or higher (illustrated in Fig. S6a). For gravity, the degree 2 to 5 power also abruptly increases for fits above degree 5, but the effect is weaker than for topography (Fig. S6b).

In our final analysis, we use the results from fitting over degrees 0 to 5, which is the minimum error solution without distortion (Fig. S4). Using the degree 0 to 4 solution produces nearly identical results and the same qualitative conclusions (shown in Table S4, discussed below). In the future, one could perform fits above degree 5 by constraining the solution to obey a certain range of power-laws. However, given the good visual agreement between the best-fit coefficients and the original data (see Figs. S4 and S7), the best-fit values are not likely to change substantially.

S2.4 - Effect of excluding different basins and the size of the basins

It is important to determine if the best-fit topography and gravity solutions are stable when certain basins are included or excluded. In particular, we are most interested in the stability of the ratio $C_{2,0}/C_{2,2}$ for uncompensated and compensated topography. Therefore, we have calculated these ratios for a number of different scenarios with basins included or excluded (listed in Table S4). We also calculated the coefficients for SPA with up to 50% larger semi-axes, and basins with up to 30% larger diameters. We find that for all scenarios including a nominally-sized or 50% larger SPA, with fits from degree 0 up to degree 3, 4 or 5, the compensated coefficients vary from -1.1 to -1.6, and the uncompensated coefficients vary from -0.5 to -1.3 (Table S4). These ranges are close to the nominal case including all 13 basins when including 1σ Monte Carlo-derived uncertainties (Table 1 and Section S2.6).

S2.5 - Fits for coefficients are approximations

The mass in SPA and other basins creates a dominantly local perturbation in the gravity potential. However, unlike for topography, removing basins from the global gravitational potential is complicated by the fact that basin mass within the boundaries we define affects the potential globally. Therefore, the calculated harmonics must be treated as approximations. However, the chosen basin boundaries enclose nearly the entire visually apparent potential anomaly, suggesting that the potential anomaly outside the boundaries is small. Furthermore, the basins' effect on the degree-2 coefficients is very modest anyway, as reflected in the small change in the location of the Moon's principal gravity axes without large basins, and the modest changes in the degree-2 gravity coefficients (a 12% change in the gravity power, compared to 44% for topography power), as discussed in the main text (e.g. Fig. 1, Table S7). In particular, SPA, which contributes 45% of the total surface area ignored, is in a state of compensation and exhibits only a weak gravity anomaly[18,24]. These modest changes imply that the uncertainty associated with the gravity coefficient approximation outside of these basins is low. Finally, it is important to mention that the new gravity terms $C_{2,1}$, $S_{2,1}$, $S_{2,2}$ (Table S6, row 3, column 2) arise from the mass effectively removed by our analysis, not from the small unaccounted-for potential outside of the basin boundaries.

An additional complication is that topography and gravity may be altered outside the boundaries we use. For example, there may be unaccounted for ejecta deposits and tectonic modifications of gravity and topography. However, the boundaries we use were chosen to account for a large fraction of the signature of the basins, and therefore are expected to be reasonable approximations. We discuss the effect of a possibly larger SPA boundary in Section S.4.

S2.6 - Monte Carlo methods to determine uncertainties in non-global spherical harmonic fits

The non-global area outside of the Moon's large basins leads to a loss of orthogonality of harmonics at different degrees, which affects the degree-2 harmonics that we seek to recover. It is critical to properly account for this effect and the uncertainties in the fitting process to determine if the estimated harmonics are sufficiently well known to make conclusions about their origins. Fortunately, we will show that the effects can be quantified and they are small enough to permit useful conclusions.

As discussed above, the fit we use is limited to a maximum of degree 5, since above degree 5 the space created by SPA begins to distort the solution. While we do not estimate the harmonics above degree 5, we would like to quantify how their variability influences our best-fit estimate of the degree 0 to 5 harmonics (since they are no longer orthogonal). The influence of these unknown higher-degree harmonics ultimately provides an uncertainty estimate for the lower degree harmonics (if the primordial pre-basin-formation Moon had only harmonics of degree 0 to 5, this would not be necessary, and a fit to degrees 0 to 5 would recover them perfectly, over a partial sphere). To quantify this effect, we produce topography maps with the best-fit coefficients from 0 to 5, plus random harmonics from degree 6 to 50. The power of the random topography harmonics from degree 6 to 50 are constrained to obey the best-fit power law when large basins are ignored (red dashed line in Fig. 1). We then perform the least-squares fitting process on the synthetic map over degrees 0 to 5, and determine the difference between the

original best-fit coefficients, and the new best-fit coefficients for the synthetic map (Fig. S7 illustrates this process). The differences between the two sets of coefficients serve as an estimate of the leakage of power from the poorly known higher degree terms, into the degree 0 to 5 terms. The process is repeated 500 times, and the variance of the differences at each degree and order, as well as the variance of the principal frame rotation angles, are used as the uncertainties in the final reported coefficients and rotation angles (listed in Tables S5 and S6). Uncertainties in the principal reference frame are obtained in a similar manner.

For the uncertainty in the gravity coefficients, the same process is used. However, since the real lunar gravity potential is strongly dependent on topography, we use the random topography coefficients from 6 to 50 to create the degree 6 to 50 gravity coefficients, based on the empirical relationship $C_{n,m,gravity} = C_{n,m,topography} \times 10^{-4}\ n^{-0.5}$ km^{-1} [the relationship produces a gravity power law with coefficients a = -2.07, b = -8.33 (compare to a = -2.04, b = -8.18 for observed gravity, Table S1)]. Using this relationship produces a map that is visually very similar to the observed gravity potential (see Fig. S7). Coupling gravity to the random topography coefficients produces slightly lower uncertainty in the final ratio of $C_{2,0}/C_{2,2}$ for uncompensated and compensated topography, since the $C_{2,0}$ and $C_{2,2}$ coefficients for each type of topography depend on both topography and gravity. In fact, to obtain the final uncertainty estimate on the ratios of $C_{2,0}/C_{2,2}$, we calculate these ratios for each of the 500 random maps, rather than calculate the errors for individual $C_{2,0}$ and $C_{2,2}$ values, and propagate those errors forward into the ratio. The reasons for this method are discussed in more detail below.

S2.7 - Uncertainty in $C_{2,0}/C_{2,2}$ ratios and gravity coefficients in topography's principal reference frame, due to non-linear propagation of error during coordinate frame rotations

A consequence of the uncertainty in the principal frame rotation angle λ for topography is that when the gravity coefficients are rotated into the topography principal frame by the same angle (see main text), there is a similar uncertainty in the required rotation angle. However, this uncertainty in the gravity data produces a much wider range of variability in the gravity coefficients $C_{2,0}$ and $C_{2,2}$, compared to topography, because there are off-diagonal degree-2 terms when the gravity data are analyzed in topography's principal frame (shown in Fig. 2e). For example, for a generic map in its principal frame with only $C_{2,0}$ = -1 and $C_{2,2}$ = 1, a rotation by $\lambda = \pm 10°$ changes the coefficients to only -0.98 and 1.01, respectively. However, with $C_{2,0}$ = -1, and $C_{2,1} = S_{2,1} = C_{2,2} = S_{2,2} = 1$, a rotation of +10° yields $C_{2,0}$ = -0.69 and $C_{2,2}$ = 1.19, which is a much larger change in $C_{2,0}$ and $C_{2,2}$ than for the case of zero non-diagonal terms. Therefore, to determine the 1σ uncertainty in $C_{2,0}$ and $C_{2,2}$ for gravity coefficients *in the topography principal reference frame* (Fig. 2e, Table 1), we use the largest and smallest coefficients produced by the largest and smallest uncertainty limits of the *topography* angle λ (which are obtained by the Monte Carlo methods in Section S2.6). We verified that the other two rotation angles θ and φ do not have as great an effect on the gravity coefficient uncertainty.

For the linear combination of uncompensated and compensated topography coefficients consistent with both gravity and topography observations (Table 1), we use the 1σ values obtained empirically by Monte Carlo methods.

In summary, while it is somewhat surprising that small uncertainties in the topography angle λ lead to large uncertainty in gravity, the uncertainties for the compensated component of topography are small enough to make conclusions about its origin. As discussed in the main text, the compensated ratio $C_{2,0}/C_{2,2}$ = -1.3 ± 0.2, has an uncertainty that spans a range of values that might be expected from tidal processes (Fig. 3). For uncompensated topography, the ratio $C_{2,0}/C_{2,2}$ is -1.0 ± 0.3. This value has a larger uncertainty, but the fact that it is equal to the value expected for a fossil bulge, even when various basins are included or excluded from the analysis (Table S4), suggests it is in fact due to a fossil bulge.

S2.8 - Principal axis locations

Table S7 gives the minimum, intermediate, and maximum principal axes for global topography, topography outside of large basins, and gravity outside of large basins (referenced to the present-day Earth-facing reference frame). Uncertainties were calculated by propagating the Monte Carlo-derived uncertainties for the individual rotation angles θ, φ, and λ (see Fig. S2).

S.3 Alternative method of estimating spherical harmonic coefficients

An alternative method to estimate the lunar gravity and topography spherical harmonic coefficients outside the largest basins is to set the topography or gravity inside the basins to the local mean outside the basins. This method has the advantage that the calculated harmonics are orthogonal and stable up to any maximum degree, but the disadvantage that creating constant-valued disk-shaped features introduces new sources of uncertainty.

To estimate the coefficients with this method, we calculated the mean topography or gravity in the region between the diameters given in Table S3, and a diameter that was either 10% or 20% larger. We then reset all values inside the basin to these mean values, and calculated the degree-2 coefficients with these new maps (shown in Figure S8). Following our methods from the previous section, we then calculated the principal frame rotation angles θ, φ, and λ for topography, rotated the topography and gravity data into the topography principal frame, and calculated the compensated and uncompensated degree-2 coefficients (shown in Table S8).

We have identified two sources of uncertainty in this procedure. The first is that even if the Moon had a perfect primordial degree-2 shape outside of these 13 basins, introducing constant-valued disk-shaped features would change the calculated degree-2 coefficients when computed globally. The second effect is that the data outside the basins are not perfect representations of the true, local primordial mean.

To quantify the first effect, we created pure degree-2 synthetic maps with the coefficients calculated by the basin filling method, then re-performed the basin filling procedure on these synthetic maps for SPA and the 12 other basins. We then calculated the differences between the synthetic input coefficients and the coefficients obtained after the filling procedure. Finally, we used the differences to correct the coefficients obtained from real lunar data (shown in Table S8).

To quantify the second effect, we calculated the mean and the standard deviation of the difference between the local real topography (or gravity) outside each basin, and the local pure

degree-2 topography (or gravity) calculated from the basin-filling method. These statistics were taken to represent a Gaussian distribution of how the local data differs from a perfect degree-2 shape. We then repeated the synthetic-map fitting procedure (previous paragraph) 1000 times, but this time adding a random component to the local topography (or gravity) values calculated outside of basins, with the same mean and standard deviation calculated in the previous step. We then took the resulting set of 1000 degree-2 coefficients and calculated their standard deviation, which we use as a rough measure of their uncertainty (shown in Table S8).

We find that the ratios for compensated and uncompensated topography are –1.4 to -1.5 ± 0.6 (1σ) and -0.8 ± 0.2 (1σ), respectively. These ratios are close to the values predicted for tidal heating and a frozen fossil-bulge, respectively, and are indistinguishable from the ratios reported in the main text, since they are within their uncertainties. Here there is higher uncertainty in the compensated topography component, perhaps because the local topography values outside of basins yield a much higher variance than for gravity (compared to a pure degree-2 sphere), and the compensated component depends more strongly on topography. Because of the higher uncertainty in the compensated topography component here, the values in the main text are preferred.

S4. Equations for compensated and uncompensated topography

To determine the tidal character of the Moon's degree-2 topography, we seek the fractions that are due to compensated and uncompensated topography, since each of these components are produced by two different mechanisms (tidal heating and a frozen tidal-rotational bulge, respectively). To do so, we use a method that analyzes the observed gravity and topography coefficients together (determined outside of large basins), as described below.

The $C_{2,m}$ gravity spherical harmonic coefficient resulting from completely compensated or completely uncompensated topography can be obtained from the relationships for top-loaded crust developed by Ojakangas and Stevenson (1989)[38],

$$C_{2,m} = Q_{2,m}\left[\left(1-C_w\right)+4C_w\,\frac{b_c}{a}\,\frac{\Delta\rho}{\rho_m}\right] \quad , \tag{S9}$$

where $Q_{2,m}$ is given by,

$$Q_{2,m} = \frac{3\rho_c t_{2,m}}{5\bar{\rho}a} \quad , \tag{S10}$$

where ρ_m is the density of the mantle (assumed 3200 kg/m^3), ρ_c is the density of the crust (assumed 2550 kg/m^3), $\bar{\rho}$ is the mean density of the Moon (assumed 3340 kg/m^3), $\Delta\rho = \rho_m - \rho_c$, here a is the mean radius (assumed 1747.2 km), $t_{2,m}$ is the crustal thickness spherical harmonic coefficient, b_c is the mean crustal thickness (assumed 40 km), and C_w is a measure of the degree of compensation.

For uncompensated topography we set C_w = 0, and in this case $t_{2,m}$ is the observed surface topography. For compensated terrain we set C_w = 1 and assume $t_{2,m} = h_{2,m}(1+\rho_c/\Delta\rho)$, where $h_{2,m}$ is the topography observed at the surface. If we use equation 2.7 from ref. 38 to estimate the value of C_w, and reasonable geophysical values for a floating early lunar crust in the magma ocean epoch (Poisson's ratio = 0.25, thickness of the lithosphere = 2 km, degree-2 rigidity = 10 GPa) we obtain C_w = 0.97, which implies that the crust will be largely compensated during this time. In reality, the case of a growing crust in the magma ocean epoch calls for a bottom-loading approach, but the implied nearly complete state of compensation justifies using the top-loading approach, which equals the bottom-loading value in the limit of complete isostasy.

The simultaneous equations to solve for the theoretical degree-2 components of compensated topography, $h_{2,m,c}$, and uncompensated topography, $h_{2,m,u}$, that produce observed topography and gravity coefficients $C_{2,m}$, are of the form

$$\begin{aligned} h_{2,m,c} + h_{2,m,u} &= C_{2,m,topo} \\ \beta h_{2,m,c} + \gamma h_{2,m,u} &= C_{2,m,grav} \end{aligned} \quad , \tag{S11}$$

where β and γ are obtained from equations S9 and S10. The solutions are:

$$h_{2,m,c} = \left[\frac{5\bar{\rho}a}{3\rho_c} C_{2,m,grav} - C_{2,m,topo}\right] \times \left[\left[1+\frac{\rho_c}{\Delta\rho}\right]\left[\frac{4b_c}{a}\frac{\Delta\rho}{\rho_m}\right] - 1\right]^{-1} \tag{S12}$$

$$h_{2,m,u} = \left[\frac{5\bar{\rho}a}{3\rho_c} C_{2,m,grav} - C_{2,m,topo}\left[1+\frac{\rho_c}{\Delta\rho}\right]\left[\frac{4b_c}{a}\frac{\Delta\rho}{\rho_m}\right]\right] \times \left[1 - \left[1+\frac{\rho_c}{\Delta\rho}\right]\left[\frac{4b_c}{a}\frac{\Delta\rho}{\rho_m}\right]\right]^{-1}$$

These solutions are used to produce the values in Table 1 and Table S9.

The ratio of gravity to topography for completely compensated or completely uncompensated terrain is shown graphically in Fig. S9. In Fig. S9 we also plot $C_{2,0}$ and $C_{2,2}$ for gravity and topography, in the topography principal frame, when ignoring large basins (from Table 1). The line that passes near both points is for an effective compensation state of 79%.

In Table S9 we show the theoretical values of topography required to produce the observed $C_{2,0}$ and $C_{2,2}$ gravity observations (outside of large basins), assuming either completely compensated, or completely uncompensated topography. The table shows that the observed topography is too low, or too high, to be explained by either completely compensated or uncompensated topography, respectively. We also show the linear combination of compensated and uncompensated topography to produce the observed topography and gravity (outside of large basins, also shown in Table 1).

S5. Topography and gravity analysis using global data

To demonstrate the effect of the Moon's large basins on our conclusions, we can calculate the uncompensated and compensated topography coefficients in the topography principal frame obtained from *global* data. Table S10 presents these calculations, analogous to Table S9, using

the coefficients and rotation angles for global topography. We find the ratios $C_{2,0}/C_{2,2}$ are -2.0 and -6.1, for compensated (crustal thickness variations) and uncompensated (fossil) topography, respectively (the uncertainties are small since the coefficients are well known). These ratios are higher than the values for known formation theories of degree-2 topography, as discussed in the main text.

S6. Crustal thickness coefficients outside of large basins

We can compare the compensated topography coefficients in the main text (Table 1) with a recent model of lunar crustal thickness derived from topography and gravity data[19] (shown in Fig. S3). The mean crustal thickness of the model is 43 km, which is slightly larger than the mean (40 km) assumed in the topography and crustal thickness calculations in the main text and Table 1. The power spectrum for this crustal thickness model is shown in Fig. S10a (see Table S1 for the power law coefficients).

To estimate the degree 0 to 5 crustal thickness coefficients outside of large basins, we used the same methods as for topography. Table S11 shows the best-fit crustal thickness coefficients and Fig. S10b shows crustal thickness in its principal frame. The angles required to rotate topography (θ = -30.5°, φ = 5.8°, λ = -35.5°) and crustal thickness data (θ = -33.4°, φ = 2.9°, λ = -52.8°) into their principal frames (ignoring large basins) are similar, consistent with the interpretation that degree-2 topography is dominated by crustal thickness contributions.

Most importantly, the ratio $C_{2,0}/C_{2,2}$ for crustal thickness in its principal frame is -1.1 ± 0.2, which is close to the value expected for strong tidal heating, as discussed in the main text. If we use *global* crustal thickness data, we find that the ratio $C_{2,0}/C_{2,2}$ in the crustal thickness principal frame is -2.2. This is higher than the values of -1.1 to -1.3 predicted in the case of strong tidal heating, emphasizing the importance of considering the Moon's large basins.

S7. Degree-4 harmonics

Tidal heating in the crust also predicts degree-4 crustal thickness variations. Therefore, comparisons of the predicted degree-4 harmonics and the observed degree-4 harmonics can help test the tidal heating model.

We find that in strong tidal-heating models (>50 mW/m^2 mean global heat flux), the largest degree-4 term is $C_{4,4}$ (positive valued), with other degree-4 terms having a lower strength by approximately an order of magnitude. The $C_{4,4}$ harmonic gives rise to the bulge-shaped features at 90° and 270° longitude in the inset map in Fig. 3. Furthermore, we find that the ratio of $C_{2,0}$ (the largest degree-2 term) to $C_{4,4}$ has a characteristic ratio of approximately -0.43 to -0.50.

Table S12 shows the degree-2 and degree-4 topography, gravity, and crustal thickness harmonics, calculated outside of SPA and large basins. We will not perform a full analysis of the degree-4 topography and gravity here, but we can make some basic observations. Firstly, in the topography principal frame, the $C_{4,4}$ topography and crustal thickness harmonics are positive and one of the larger degree-4 terms. Secondly, $C_{2,0}/C_{4,4}$ = –0.28 ± 0.14 (1σ) for crustal thickness, in the topography principal frame. This ratio is the correct sign and marginally

supportive of the tidal heating hypothesis, given its uncertainty. It is possible that a number of events may have taken place that altered the degree-4 harmonics, with less of an effect on the degree-2 harmonics. For example, erosion of degree-4 surface features due to large impacts or relaxation due to lower crustal flow may take place more rapidly than at degree-2. A more complete analysis of the degree-4 terms can be performed in a future study.

S8. Tidal heating calculations

S8.1 - Methods and results

To determine the range of $C_{2,0}/C_{2,2}$ for crustal thickness (or compensated topography) patterns that result from tidal heating in a crust floating over a magma ocean, we used the same methods described in Garrick-Bethell et al. (2010)[16]. Briefly, we solve for the quasi-equilibrium structure of a dry anorthositic crust with a temperature-dependent viscosity profile, undergoing tidal deformation and basal heating from below, while including the effects of surface insolation.

The amount of dissipation in the crust depends on the orbital eccentricity, orbital semi-major axis, the mean thickness of the crust at the time of the modeled dissipation, the basal heat flux from background heat sources (which, in conjunction with the tidal heat flux, controls the mean thickness), the viscosity structure of the crust, and the temperature profile of the crust (which we assume controls the viscosity). A number of unmodeled effects can have a large influence on the viscosity, and in turn the amount of dissipation, such as the amount of interstitial melt in the lower crust, the amount of water in the crust, and uncertainties in the anorthosite flow law that we assumed in Garrick-Bethell et al. (2010)[16]. In order to simplify the analysis, our goal is to determine the shape of the crust for the extremes of almost no dissipation and high dissipation. To quantify the amount of dissipation, we calculate the global mean tidal heat flux. We choose a fixed semi-major axis of 20 Earth radii, and vary the eccentricity between 0.02-0.03 to decrease or increase dissipation, respectively (the current mean eccentricity is 0.055 and is increasing). We also varied the background basal heat flux from 20 – 40 mW/m^2. Garrick-Bethell et al. (2010)[16] estimated the primordial basal heat flux was ≈30 mW/m^2, compared to today's global mean ≈10 mW/m^2.

The values we used for the basal temperatures (which set the viscosity of the base of the crust) range up to 1450° C, which is an extreme value that is likely too high for a lunar magma ocean during crystallization. However, changes in temperature provide an easy means of altering the viscosity structure of the crust, in order to test the limits of zero to high dissipation, and obtain the function $C_{2,0}/C_{2,2}$ vs. global mean tidal heat flux.

One of the results we report is the mean equilibrium crustal thickness. However, because crustal thickness growth may have continued after dissipation was important, the mean thickness reported here is not as relevant for comparison with the present day Moon as the $C_{2,0}/C_{2,2}$ ratio. The magnitudes of the coefficients are also important, but with the caveat that when tidal dissipation decreases, high coefficient values can become muted as crystallization of crust and mantle materials continue in an ocean with degree-2 depth variations.

Figure 3 shows that for very low dissipation (mean tidal heat flux < 1 mW/m^2), the ratio $C_{2,0}/C_{2,2}$ is positive, which results from positive $C_{2,0}$ and $C_{2,2}$ values (Table S13). The positive $C_{2,0}$ results from the effect of insolation: at the poles the lower temperature leads to higher crustal thickness (by a small amount), which is the opposite sign of crustal thickness variations from tidal heating. If the crustal thickness under these conditions was solely responsible for the moments of inertia, the Moon would reorient to distribute this mass excess to the equator, and create a negative ratio $C_{2,0}/C_{2,2}$ in the new reference frame. (As an example of this, a planet with only a harmonic $C_{2,0}$ = +1, rotated 90° in latitude to the equator will then have $C_{2,0}$ = -0.5, and $C_{2,2} = 3^{1/2}/2$). For tidal dissipation cases that are strong enough to overcome this weak insolation effect, the value of $C_{2,0}/C_{2,2}$ quickly reaches a negative minimum at ≈5 mW/m^2, and then increases to approximately -1.1 to -1.3 above ≈50 mW/m^2.

Table S13 shows the assumed eccentricity, basal background heat flux, and basal crustal temperature, and the resulting shape and global mean tidal heat flux values for 114 model calculations. Note that not all temperature/eccentricity combinations were calculated, due to some numerical limitations. Tidal heat fluxes >225 mW/m^2 are difficult to produce with reasonable parameters, and have not been calculated.

The result in Fig. 3 (case 38 in Table S13) is based on model calculations with a basal crust temperature of 1350°C, but other cases have $C_{2,0}/C_{2,2}$ values close to the proper ratio for temperatures near 1200°C. For example, case 87 has a ratio $C_{2,0}/C_{2,2}$ = -1.15, with a basal temperature of 1200°C. Ilmenite, a mineral which forms after ≈95% of magma ocean crystallization, is expected to crystallize at 1125-1180°C (ref. 39), and therefore it is plausible that temperatures were >1200°C early in magma ocean crystallization (which is also when the Moon would have been closer to the Earth, and tidal deformations would have been higher). Again, there may also be other effects that increase the dissipation or viscosity that we have not modeled.

Regardless of the precise conditions, it is evident that significant tidal heating can take place within a range of plausible parameters of the early Moon, and that the crustal structure of the Moon is consistent with that process.

S8.2 – Lower crustal flow

It is important to consider how early degree-2 crustal thickness differences may have been moderated by lower crustal flow after tidal heating ceased. Similar calculations have been performed for tidally-produced ice shell thickness differences on Europa[40-42]. Previously, Garrick-Bethell et al. (2010)[16] (their Supporting Online Material Section 6) found that significant crustal flow was not likely to take place in less than 150 By. In those calculations, they used a creep flow law from Rybacki and Dresen (2000)[43], with stress exponent n = 3 (indicating non-Newtonian dislocation creep), and an assumed basal temperature of 1175° C. However, in the present study, we calculated tidal heating cases with higher temperatures (Table S13). As described in the main text and Section S8.1, there are many uncertainties in the properties of the early crust, and while some temperatures we use may not be achieved, they illustrate the effect of progressively higher tidal heat fluxes on the shape parameters $C_{2,0}$ and $C_{2,2}$.

Before we calculate the timescale for crustal flow at temperatures >1175° C, we will establish that the flow law used previously for anorthosite is appropriate. We assume a strain rate $\dot{\epsilon}$,

$$\dot{\epsilon} = A\sigma^n d^{-m} e^{(-Q/(RT_b))} \quad \text{(S13)}$$

where here A, Q, n, and m are rheological constants that depend on the flow law, R is the gas constant, T_b is temperature (K), σ is stress, and d is the grain size. Rybacki and Dresen (2000)[43] found that dry anorthosite likely flows via diffusion (Newtonian flow n = 0, m = 3) or dislocation creep (non-Newtonian, n = 3, m = 0), depending on σ and T. The driving stress for crustal flow is $\approx \Delta\rho hg$, where here $\Delta\rho$ is the crust-ocean density contrast, h is the thickness contrast, and g is gravity. For $\Delta\rho$ = 300 kg/m^3 and h = 10 km, $\sigma \approx$ 5 MPa.

To determine which flow law dominates for σ = 5 MPa and T_b = 1350° C (e.g. tidal heating case 38, main text, Table S13), we calculate $\dot{\epsilon}$ for dislocation and creep flow laws, assuming d = 1000 μm (appropriate for mid to lower crustal rocks), Q = 648 kJ/mol and $\log_{10}(A)$ = 12.7 MPa^{-n} s^{-1} (for dislocation creep), and Q = 467 kJ/mol and $\log_{10}(A)$ = 12.1 MPa^{-n} μm^m s^{-1} (for diffusion creep). We find that for all σ > 0.1 MPa, $\dot{\epsilon}$ for dislocation creep is higher than for diffusion creep (at 0.1 MPa and 10 MPa, $\dot{\epsilon}$ is greater by two and five orders of magnitude, respectively). Because the strain rate for dislocation creep is higher at the relevant stresses and temperatures, our use of the dislocation creep (n = 3, m = 0) flow law is appropriate. This is also the flow law used in our tidal heating calculations.

Equation S8 of Garrick-Bethell et al. (2010)[16] (or eq. A.10 of ref. [42]) gives the time for a crustal thickness contrast to relax by 1/e, assuming non-Newtonian flow. The equation assumes flow takes place in a channel of thickness δ. Previously, Garrick-Bethell et al. (2010)[16] assumed a channel thickness related to the e-folding scale of temperature (and viscosity):

$$\delta = \frac{RT_b^2 D_m}{Q(T_b - T_s)} \quad \text{(S14)}$$

where T_s is the surface temperature and D_m is the mean crustal thickness. This expression assumes a linear crustal temperature gradient and yields δ = 0.4 km for D_m = 17.8 km (the value for case 38), using Q = 648 kJ/mol, T_b = 1350° C, and T_s = -20° C. In Figure S11 we plot the model crustal temperature profile for case 38 from Table S13. At the base of the crust, where the majority of tidal dissipation takes place, the temperature gradient is steeper than in the rest of the crust. The thickness of this layer is ≈1.5 km. Therefore, we use δ = 1.5 km instead of 0.4 km. This yields 2.6 By for the 1/e crustal thickness difference relaxation time, assuming an initial crustal thickness contrast of 20 km (conservatively high). As the crust eventually cools, the timescale will increase quickly, such that this timescale estimate is conservatively low. This timescale is shorter than the 150 By timescale originally reported in Garrick-Bethell et al. (2010)[16], but ultimately, the crustal flow timescale must only be shorter than the time until the lithosphere gains strength at degree-2. We have shown that this takes place at ≈30-32 Earth radii, or nominally ≈200-300 My after accretion (main text). Therefore, in light of the order of magnitude difference between the crustal relaxation timescale and the time until lithosphere development, we conclude that the modeled crustal thickness contrasts will persist after tidal heating ceases. If the starting basal temperature was lower, it would further increase the timescale for crustal flow.

S9. – Statistics of the lunar topography coefficients

S9.1 – Topography statistics

We would like to assess the possibility that the ratios $C_{2,0}/C_{2,2}$ for compensated and uncompensated topography are equal to their predicted ratios by chance. For example, one might initially guess that the mean ratio between all harmonics is close to unity. To help answer this question we first determine: 1) The natural distribution of the ratio of all other zonal harmonics (harmonics $C_{n,0}$), to the even tesseral harmonics of the same degree, with even order m, and same index type C (*i.e*, we find the ratios of $C_{3,0}/C_{3,2}$, $C_{4,0}/C_{4,2}$, $C_{4,0}/C_{4,4}$, etc.), and 2) Assuming a set of $C_{2,0}/C_{2,2}$ ratios sampled from this distribution, what is the $C_{2,0}/C_{2,2}$ ratio distribution after rotating to the principal frame? The second question is important because while in an arbitrary reference frame the ratio $C_{n,0}/C_{n,m}$ may be any value (see below), not all ratios of $C_{2,0}/C_{2,2}$ are allowed in the principal frame, which we use in the text. This is because some initial $C_{2,0}$ and $C_{2,2}$ values will result in the largest moment of inertia being in a non-polar axis, which would result in polar wander, and thereafter a different $C_{2,0}/C_{2,2}$ value. The criteria for this reorientation are, in normalized harmonics (Ojakangas and Stevenson (1989)[38] eq. 3.2-3.4),

$$\begin{aligned} I_{xx} > I_{zz} \;:\; C_{2,0} - \sqrt{1/3}C_{2,2} > 0 \\ I_{yy} > I_{zz} \;:\; C_{2,0} + \sqrt{1/3}C_{2,2} > 0 \quad , \end{aligned} \tag{S15}$$

where I_{xx}, I_{yy}, and I_{zz} are the moments of inertia about the Earth-Moon line, orbit-tangent line, and polar axis, respectively. For unnormalized harmonics, the coefficient in front of $C_{2,2}$ becomes 2.

Figure S12a shows the distribution of the $C_{n,0}/C_{n,m}$ ratios for lunar topography (up to degree 50, no basin corrections) is Gaussian-like, except with a large number of ratios close to zero. The standard deviation of the best-fit Gaussian of the distribution is 1.10, and the mean is -0.06, which we take to be zero.

If we take 10,000 random samples from the observed lunar $C_{n,0}/C_{n,m}$ distribution, use these values as $C_{2,0}/C_{2,2}$ (assuming it would be similarly distributed), and determine the new topography $C_{2,0}/C_{2,2}$ ratios in the implied principal frame, we obtain the distribution in Fig. S12b. The ratios are always negative, as expected, and have an upper limit at $-(1/3)^{1/2}$ (= -0.58), which comes from the criteria for reorientation (eq. S15).

S9.2 – Gravity statistics

We wish to also understand the statistics of the Moon's gravity harmonics, such that we can calculate the $C_{2,0}/C_{2,2}$ ratio statistics for the compensated and uncompensated topography components. However, this is complicated by the fact that gravity is partially correlated with topography, and partially random. To address this, we sample topography $C_{2,0}$ and $C_{2,2}$ values from the distribution in Fig. S12b, and then create $C_{2,0}$ and $C_{2,2}$ gravity terms with the same topography to gravity ratio as observed for the actual basin-removed degree-2 terms (*i.e*. for $C_{2,0}$

this ratio is: 0.65 km / 4.3×10^{-5}, and for $C_{2,2}$ the ratio is: 0.51 km / 3.9×10^{-5}). An additional random gravity component is then added to the gravity terms $C_{2,0}$, $C_{2,2}$, as well as $C_{2,1}$, $S_{2,1}$, and $S_{2,2}$ terms, such that on average, the total degree-2 gravity power is equal to the total observed basin-removed power (= 8.4×10^{-9}, Fig. 1, Table S6). The standard deviation of this generated degree-2 gravity power is 3.8×10^{-9}, which we consider small enough to be a good approximation for the actual Moon. On average, 36% of the generated gravity power is found in terms with zero topography (*i.e.* $C_{2,1}$, $S_{2,1}$, and $S_{2,2}$), which of the same order as for the basin-removed Moon (59%, main text). The lower percentage in the simulation actually provides more conservative statistics (below), since the implied tighter correlation between topography and gravity in the simulation improves the odds that the ratios will assume their tidally predicted values. That is, it would be extremely fortuitous to find gravity and topography that provide the predicted coefficient ratios for compensated and uncompensated topography, if both topography and gravity were totally uncorrelated (two random variables), but less fortuitous if they were 100% correlated (one random variable).

Note that we also scale the topography harmonics to their observed basin-removed power before these operations (= 0.67 km^2, Fig. 1, Table S5).

S9.3 – Uncompensated and compensated topography coefficients

When the compensated topography coefficients are calculated from the topography and gravity coefficient distributions generated above (using equation S12), we find that the probability of obtaining a compensated topography $C_{2,0}/C_{2,2}$ ratio between -1.1 to -1.3 is 8% (Fig. S13a). Figure S13a reveals a small number of *positive* $C_{2,0}/C_{2,2}$ values. The input topography ratios from Fig. S12b are always negative, but the calculated compensated topography ratios are sometimes positive because the compensated component of topography is physically weakly dependent on gravity (*i.e.* large changes in gravity can be explained by small changes in *uncompensated* topography), and some extreme gravity values occasionally produce positive ratios.

For uncompensated topography, we find the fraction of $C_{2,0}/C_{2,2}$ ratios between -0.9 and -1.1 is 5% (Fig. S13b). This probability is smaller than for the compensated ratios, since the uncompensated component is physically more strongly dependent on gravity. Therefore, this ratio is essentially dependent on *two* random variables: topography and gravity (with gravity constructed on average to be about 64% correlated with topography, described above). This gravity dependence can also be seen in the higher abundance of positive ratios in the uncompensated topography $C_{2,0}/C_{2,2}$ ratio distribution (Fig. S13b), compared with the compensated distribution (Fig. S13a).

Note that it would not be appropriate to perform any coordinate system rotations on the positive-valued ratios to make them negative (negative ratios imply moments of inertia that would lead to polar wander, Section S9.1), since all of these values were already derived from *total* topography with $C_{2,0}/C_{2,2}$ ratios that are negative (Fig. S12b).

Finally, we find the probability of finding both compensated and uncompensated $C_{2,0}/C_{2,2}$ ratios in their respective ranges is 0.3%, which we report in the main text. This probability is slightly

lower than the simple 0.08 × 0.05 calculation that assumes the two probabilities combine linearly.

S10. Alteration of the degree-2 shape by subsequent processes

S10.1 - Spherical cap gravity anomaly

In Section 9 we established that the Moon's tidal signature would rarely be produced by random processes. If the Moon's topography was sculpted by tides, we can also estimate the probability of witnessing it today, in spite of the additional gravity power added after its formation (main text). If this probability is reasonable, it further supports the hypothesis that the Moon's degree-2 topography is tidal in origin. To do so, we created gravity maps using just the Moon's $C_{2,0}$ and $C_{2,2}$ gravity harmonics outside of large basins (Fig. 2e), and added a randomly placed half-sphere gravity anomaly cap of constant value (1.5×10^{-4}). As discussed in the main text, a spherical cap is a reasonable first-order approximation for the process that may have contributed power to the Moon's degree-2 gravity field. The amplitude of the cap anomaly was chosen so that on average, the total degree-2 gravity power is equal to the observed degree-2 power outside of large basins (8.4×10^{-9}, Table S6). We then recomputed the degree-2 harmonics for 5000 test cases, and calculated the compensated and uncompensated topography $C_{2,0}/C_{2,2}$ ratios (equation S12), using the $C_{2,0}$ and $C_{2,2}$ values for topography (see Fig. 2d).

The results of these calculations are that the compensated topography ratio $C_{2,0}/C_{2,2}$ survives 92% of the time, while the uncompensated ratio survives 37% of the time, assuming that survival is a ratio change of less than 30% (reported in the main text). While the latter survival rate is somewhat low, it is certainly high enough that it is plausible the Moon's tidal signature could have survived for us to observe. A different model for the anomaly may produce different values. Again, for Moons derived from totally random sets of topography and gravity (Section S9), very few would have ratios that fall close to the observed values, which implies tidally-produced ratios did in fact survive the gravity anomaly's formation.

Because the Moon's topography, as opposed to just gravity, is a key portion of the calculation of the ratio $C_{2,0}/C_{2,2}$ for each type of topography (compensated or uncompensated), the survival rate is fairly high when new gravity power is added. Finally, the degree-2 gravity anomaly we model here also has the advantage of producing some degree-1 topography power, which is observed in the real Moon (via the center-of-mass/center-of-figure offset).

S10.2 - Mantle convection

One particular phenomenon that could have altered the degree-2 tidal shape is mantle convection. While mantle convection could not have altered the shape during the magma ocean epoch, it could have plausibly affected it after the crust crystallized, and the lithosphere started to form. We briefly consider four process by which mantle convection could affect topography: 1) Dynamically produced topography due to present-day mantle convection, 2) Dynamically produced topography during early mantle convection that "froze-in" and persisted until the present day, 3) Density contrasts formed by mantle convection that froze-in at depth, but only influenced the gravity field, and 4) Crustal thickness changes produced by mantle convection.

Given the low probability of a random process generating the Moon's unique degree-2 shape (0.3%, Section S9), none of these processes are likely to be important. However, for completeness we briefly outline the physical properties associated with each of them.

The first process is unlikely to operate, given the large thickness of the present lithosphere (>700 km, e.g. refs. 44,45) and its expected strength at degree-2 (ref. 24). That is, if the present lithosphere is able to support degree-2 topography loads[24], it is also able to prevent the expression of degree-2 topography from internal convective stresses. This mechanism was originally proposed by Cassen and Young (1978)[46], but it can now be dismissed with our understanding of the Moon's lithosphere. It is also unlikely that the lunar mantle is presently convecting.

With regard to the second process, it is plausible that if there was degree-2 power in the early mantle convection pattern, it could have produced dynamic degree-2 topography and geoid (gravity) anomalies. In addition, it is plausible that these anomalies could have "frozen-in" as the lunar lithosphere formed. Buck and Parmentier (1986)[47] suggested a similar process could produce small-scale gravity anomalies in the oceanic lithosphere. However, it is not certain when the mantle began to convect and whether or not the lithosphere would have resisted deformation at that time. For example, Parmentier et al. (2002)[48] predict a ≈500 My timescale for convective overturn, while large mantle plumes develop more quickly in Zeithe et al. (2009)[49]. Zhong and Zuber (2000)[24] predict that even a 100-My-old lithosphere could resist degree-2 loads. Also, this mechanism requires that the convection pattern remain constant as the lithosphere freezes. In sum, this mechanism in principle has the potential to influence the lunar shape, but is not supported by the statistically unique coefficient ratios that suggest that tides are the cause of the degree-2 shape. In fact, our findings and the timescales they represent may help constrain early thermal processes like mantle convection.

With regard to the third process, it is possible that density changes could have arisen from processes related to convection, and frozen into the Moon to produce power in the degree-2 gravity field. We have already considered the possibility that the degree-2 characteristics would still be recoverable in the case of a cap-shaped pure gravity anomaly (*i.e.* with no topography, Section S10.1). Therefore, even if this process took place, and a cap-shaped anomaly is a reasonable approximation for the resulting density contrasts, it is unlikely to affect our conclusions. Also, as we have already argued, the unique degree-2 coefficients can only rarely be produced by random processes.

With regard to the fourth process, crustal thickness patterns influenced by convection have been proposed to explain the degree-1 Mars crustal thickness dichotomy[50,51]. However, the details of how crustal thickness could change due to convection patterns are not well established[50], and therefore whether or not they would apply to the Moon is uncertain. In addition, the lunar lithosphere grows quickly, such that these processes might operate at depth, but merely produce density anomalies (as in the process described above), instead of compensated crustal thickness changes. Therefore, as for the second case, there is potential for this process to have operated on the Moon, but statistical arguments do not support their significant contribution to the degree-2 shape.

S11. Tidal despinning timescale

An assumption in our analysis is that the Moon spun down to the synchronous state before the crust and lithosphere developed. Using equations for tidal despinning timescales[52,53], we find that for any semi-major axis $a < 5$ Earth radii, the tidal despinning time is < 100 years, assuming an initial spin period of 5 hours, $k_2 = 1.5$, and $Q = 100$. This timescale is significantly shorter than the expected formation times for the crust and eventually the lithosphere.

S12. Thorium map

Figure S14 shows a map of the near-surface thorium distribution from Lunar Prospector data.

S13. Data sources

Lunar gravity data are from a 660 degree and order GRAIL expansion obtained from data at http://pds.nasa.gov.

Lunar topography data are from the Lunar Reconnaissance Orbiter Lunar Laser Altimeter, sampled at 4 pixels per degree, *i.e.* 1/4° resolution (http://imbrium.mit.edu).

Lunar crustal thickness data are from Model 3 from http://www.ipgp.fr/~wieczor/GRAILCrustalThicknessArchive/GRAILCrustalThicknessArchive.html

Reflectance data for Fig. 1 are from Clementine data available at http://www.mapaplanet.org/explorer/moon.html.

Lunar thorium data are from a 0.5-degree resolution map available at http://www.mapaplanet.org/explorer/moon.html.

Section S1 uses data from Venus, Earth, and Mars. Topography data for Mars are from a 90 degree and order expansion from the Mars Orbiter Laser Altimeter (http://starbase.jpl.nasa.gov/). Gravity data for Mars data are from 110 degree and order expansion from Mars Reconnaissance Orbiter tracking data (http://pds-geosciences.wustl.edu). The topography data for Venus are from a 719 degree and order expansion from Magellan, Pioneer Venus and Venera 15/16 altimetry (http://www.ipgp.fr/~wieczor/SH/SH.html). Venus gravity data are from the 180 degree and order expansion of a Magellan model (http://pds-geosciences.wustl.edu). The topography data for the Earth are from a 2160 degree and order spherical harmonic model (http://www.ipgp.fr/~wieczor/SH/SH.html). Gravity data for the Earth are from the 60 degree and order static GRACE model (ftp://podaac-ftp.jpl.nasa.gov).

S14. Note on significant figures in Supplementary Information

In some cases in the SI we show one extra significant figure for bookkeeping. However, in any case where an uncertainty is reported, the decimal place of the uncertainty should be taken as the least significant figure. In the main text, only formal least significant figures are shown.

S15. Map projections used

All maps shown in the main text and SI use the Mollweide projection.

SI References

31 Wieczorek, M. A. Gravity and topography of the terrestrial planets. *Treatise on Geophysics* **10**, 165-206 (2007).

32 Kaula, W. M. *Theory of Satellite Geodesy*. 124 (Blaisdell Publishing Company, 1966).

33 Phillips, R. & Lambeck, K. Gravity fields of the terrestrial planets: Long-wavelength anomalies and tectonics. *Rev. Geophys. Space Phys.* **18**, 27-76 (1980).

34 Yoder, C. F., Konopliv, A. S., Yuan, D.-H., Standish, E. M. & Folkner, W. M. Fluid core size of Mars from detection of the solar tide. *Science* **300**, 299-303 (2003).

35 Yoder, C. F. in *Global Earth Physics, A Handbook of Physical Constants, AGU Reference Shelf Series, vol. 1, ed. T. J. Ahrens* (AGU, 1995).

36 Zuber, M. T. & Smith, D. E. Mars without Tharsis. *J. Geophy. Res.* **102**, 28673-28686 (1997).

37 Lambeck, K. *The Earth's Variable Rotation: Geophysical Causes and Consequences*. 449 (Cambridge Univ. Press, 1980).

38 Ojakangas, G. W. & Stevenson, D. J. Polar wander of an ice shell on Europa. *Icarus* **81**, 242-270 (1989).

39 Elkins-Tanton, L. T., Burgess, S. & Yin, Q.-Z. The lunar magma ocean: Reconciling the solidification process with lunar petrology and geochronology. *Earth Planet. Sci. Lett.* **304**, 326-336 (2011).

40 Stevenson, D. J. Limits on the variation of thickness of Europa's ice shell. *Proc. Lunar Planet. Sci. Conf. 31st*, Abstract 1506 (2000).

41 Nimmo, F. Non-Newtonian topographic relaxation on Europa. *Icarus* **168**, 205-208 (2004).

42 Nimmo, F., Pappalardo, R. T. & Giese, B. On the origins of band topography, Europa. *Icarus* **166**, 21-32 (2003).

43 Rybacki, E. & Dresen, G. Dislocation and diffusion creep of synthetic anorthite aggregates. *J. Geophy. Res.* **105**, 26,017-026,036 (2000).

44 Spohn, T., Konrad, W., Breuer, D. & Ziethe, R. The longevity of lunar volcanism: Implications of thermal evolution calculations with 2D and 3D mantle convection models. *Icarus* **149**, 54-65 (2001).

45 Konrad, W. & Spohn, T. Thermal history of the moon - Implications for an early core dynamo and post-accretional magmatism. *Adv. Space Res.* **19**, 1511-1521 (1997).

46 Cassen, P. & Young, R. E. The distortion of the Moon due to convection. *Geophs. Res. Lett.* **5** (1978).

47 Buck, W. R. & Parmentier, E. M. Convection beneath young oceanic lithosphere: Implications for thermal structure and gravity. *J. Geophy. Res.* **91**, 1961-1974 (1986).

48 Parmentier, E. M., Zhong, S. & Zuber, M. T. Gravitational differentiation due to initial chemical stratification: origin of lunar asymmetry by the creep of dense KREEP? . *Earth Planet. Sci. Lett.* **201**, 473-480 (2002).

49 Ziethe, R., Seiferlin, K. & Hiesinger, H. Duration and extent of lunar volcanism: Comparison of 3D convection models to basalt ages. *Planetary and Space Science* **57**, 784-796 (2009).
50 Roberts, J. H. & Zhong, S. Degree-1 convection in the Martian mantle and the origin of the hemispheric dichotomy. *J. Geophy. Res.* **111**, E06013 (2006).
51 Zhong, S. & Zuber, M. T. Degree-1 mantle convection and the crustal dichotomy on Mars. *Earth and Planetary Science Letters* **189**, 75-84 (2001).
52 Goldreich, P. & Soter, S. Q in the solar system. *Icarus* **5**, 375-289 (1966).
53 Murray, C. D. & Dermott, S. F. *Solar system dynamics*. (Cambridge University Press, 2000).

Table S1. Best-fit power-law coefficients for gravity and topography power W (eq. S4), for a fit to degrees 3 to 50. Units are in $\log_{10}$ units of W/degree (a) and W (b).

	Venus		**Earth**		**Mars**		**Moon**		**Moon (without large basins)***	
	a	*b*	*a*	*b*	*a*	*b*	*a*	*b*	*a*	*b*
Topography	-1.89	0.27	-1.78	0.87	-1.83	0.76	-1.35	0.07	-1.10	-0.30
Gravity	-3.36	-9.19	-2.99	-9.96	-2.73	-7.86	-2.14	-8.04	-2.04	-8.18
Crustal thick.							-0.92	1.23	-0.79	1.03

*Using best-fit degree 3, degree 4, and degree 5 values outside of large basins (Tables S5, S6, S9, and S11).

Table S2. Ratio of non-hydrostatic degree-2 power to the power predicted at degree-2 from a best-fit power law (fit to degrees 3 to 50).

	Venus	**Earth**	**Mars**	**Mars (without Tharsis)**	**Moon**	**Moon (without large basins)***
Topography	0.11	0.29	1.58	0.23	2.62	2.8
Gravity	0.07	4.41	6.41	0.48	4.52	5.2

*Using predictions from best-fit power law and observed power outside of large basins (Tables S5 and S6).

Table S3. Basin boundaries and centers.

Basin name	**Center (Lat.°, Long.° E)**	**Diameter (km)**
1. South Pole-Aitken	(-53.2°, 191°)	a = 2400, b = 2060*
2. Imbrium	(34°, 343°)	1150
3. Orientale	(-19°, 266°)	900
4. Nectaris	(-15.2°, 34.5°)	850
5. Serenitatis	(27°, 19°)	700
6. Crisium	(17°, 58.4°)	600
7. Mendel-Rydberg	(-50°, 266°)	600
8. Freundlich-Sharonov	(18.5°, 175.5°)	550
9. Hertzsprung	(2.0°, 231°)	550
10. Humboldtianum	(57.5°, 82°)	550
11. Humorum	(-24.4°, 321.4°)	550
12. Moscoviense	(26.5°, 147.9°)	550
13. Smythii	(-1.5°, 87.5°)	500

*Here a = 2 × semi-major axis, b = 2 × semi-major axis. The basin also has a tilt angle = -18.8°. The angle is measured clockwise from a meridian through the basin center[17].

Table S4. Compensated and uncompensated topography ratios $C_{2,0}/C_{2,2}$, calculated using topography and gravity data outside of the basins shown, for fits over degrees 0 to 4 and degrees 0 to 5. For the cases with SPA with semi-axes 10% and 20% larger than the nominal values, the degree 5 solutions start to become unstable (due to the increased size of SPA), and we only report the degree 4 solutions (or degree 3 for semi-axes > 20% larger than nominal).

	Up to degree 4		**Up to degree 5**	
Basins excluded from spherical harmonic fit*	**Comp. topo. $C_{2,0}/C_{2,2}$**	**Uncomp. topo. $C_{2,0}/C_{2,2}$**	**Comp. topo. $C_{2,0}/C_{2,2}$**	**Uncomp. topo $C_{2,0}/C_{2,2}$**
None (global data, Table S10)	-2.0	-6.1	-2.0	-6.1
I	-1.9	-6.3	-1.9	-6.1
O	-2.3	-6.5	-2.3	-6.3
N	-1.9	-7.3	-1.9	-7.9
SPAm20	-1.4	-2.0	-1.5	-2.6
SPAm10	-1.3	-1.3	-1.3	-1.4
SPAp10	-1.4	-0.6		
SPAp20	-1.6	-0.5		
SPA	-1.3	-0.8	-1.2	-0.6
SPA, I	-1.2	-0.8	-1.2	-0.6
SPA, I, N	-1.2	-0.7	-1.2	-0.6
SPA, I, O	-1.3	-1.2	-1.2	-1.2
SPA, I, O, N,	-1.3	-1.1	-1.2	-1.3
SPA, I, O, N, Sr	-1.2	-1.3	-1.1	-1.3
SPA, I, O, N, Sr, C	-1.2	-1.3	-1.1	-1.3
SPA, I, O, N, Sr, C, MR	-1.3	-1.0	-1.2	-1.0
SPA, I, O, N, Sr, C, MR, FS	-1.3	-1.1	-1.3	-1.0
SPA, I, O, N, Sr, C, MR, FS, Hz	-1.3	-1.3	-1.2	-1.2
SPA, I, O, N, Sr, C, MR, FS, Hz, Ht	-1.4	-1.1	-1.3	-1.0
SPA, I, O, N, Sr, C, MR, FS, Hz, Ht, Hr	-1.4	-1.1	-1.3	-1.0
SPA, I, O, N, Sr, C, MR, FS, Hz, Ht, Hr, Ms	-1.5	-1.1	-1.4	-0.9
SPA, I, O, N, Sr, C, MR, FS, Hz, Ht, Hr, Ms, S†	-1.5	-1.1	-1.3	-1.0
SPAp10, I, O, N, Sr, C, MR, FS, Hz, Ht, Hr, Ms, S	-1.5	-1.1		
SPAp20, I, O, N, Sr, C, MR, FS, Hz, Ht, Hr, Ms, S	-1.6	-1.0		
All 13 basins with 20% larger boundaries	-1.5	-0.9		
All 13 basins with 30% larger boundaries	-1.5	-0.8		
	Up to degree 3			
12 basins with 30% larger boundaries, SPA +40%‡	-1.0	-1.0		
12 basins with 30% larger boundaries, SPA +50%‡	-0.9	-1.3		

*Abbreviations: SPA = South Pole-Aitken basin, SPAm10, 20 = SPA with 10% or 20% smaller semi-axes, respectively, SPAp10, 20 = SPA with 10% or 20% larger semi-axes, respectively, I = Imbrium, O = Orientale, N = Nectaris, Sr = Serenitatis, C = Crisium, MR = Mendel-Rydberg, FS = Freundlich-Sharonov, Hz = Hertzsprung, Ht = Humboldtianum, Hr = Humorum, Ms = Moscoviense, S = Smythii.
†Degree-5 fit used in the main text and for all conclusions.
‡Percentage given for SPA indicates increase in its nominal boundary size.

Table S5. Topography spherical harmonic coefficients calculated outside SPA and 12 large basins, fit up to degree 5, in the present Earth-facing frame and the principal frame. Coefficients derived from global data in the present frame are also shown. $W(n)$ is the power for degree n (eq. S3) (km^2) (equal in the principal and present frames). The angles for rotation of topography into its principal frame using global data, and using data outside SPA and large basins, are shown at the bottom. Uncertainties are derived from Monte Carlo analysis. Coefficients used in analysis in main text are highlighted.

	Global data, present frame, km		**Fit outside basins, present frame, km (± 1σ)**		**Fit outside basins, principal frame, km (±1σ)**	
Degree, Order	***C***	***S***	***C***	***S***	***C***	***S***
0,0	-0.248*		0.24 ± 0.09		0.24 ± 0.09	
1,0	0.138		-0.28 ± 0.11		-0.49 ± 0.06	
1,1	-1.025	-0.422	-1.35 ± 0.09	-0.51 ± 0.03	-1.38 ± 0.11	-0.05 ± 0.06
$W(1)$	1.24		2.2 ± 0.2			
2,0	-0.668		-0.45 ± 0.06		-0.65 ± 0.05	
2,1	-0.769	-0.017	-0.27 ± 0.09	0.18 ± 0.03		
2,2	0.109	0.383	0.26 ± 0.03	0.54 ± 0.03	0.51 ± 0.05	
$W(2)$	1.20		0.67 ± 0.06			
3,0	0.063		0.00 ± 0.05		0.00 ± 0.10	
3,1	0.553	0.088	0.14 ± 0.11	0.00 ± 0.04	0.25 ± 0.12	0.17 ± 0.04
3,2	0.438	0.189	0.22 ± 0.09	0.01 ± 0.05	0.24 ± 0.06	0.01 ± 0.04
3,3	0.406	-0.006	0.32 ± 0.04	-0.01 ± 0.03	0.05 ± 0.03	-0.14 ± 0.03
$W(3)$	0.70		0.17 ± 0.04			
4,0	0.216		0.17 ± 0.05		0.04 ± 0.07	
4,1	-0.225	-0.048	0.02 ± 0.08	-0.01 ± 0.04	0.05 ± 0.13	0.05 ± 0.05
4,2	-0.327	-0.101	-0.04 ± 0.08	0.01 ± 0.06	-0.22 ± 0.06	-0.15 ± 0.09
4,3	-0.199	-0.287	-0.06 ± 0.05	-0.22 ± 0.05	-0.05 ± 0.03	0.05 ± 0.04
4,4	-0.192	0.111	-0.11 ± 0.03	0.12 ± 0.02	0.11 ± 0.05	-0.11 ± 0.03
$W(4)$	0.39		0.11 ± 0.02			
5,0	0.115		-0.08 ± 0.04		0.03 ± 0.07	
5,1	0.029	-0.033	-0.04 ± 0.06	-0.03 ± 0.02	-0.09 ± 0.06	-0.06 ± 0.06
5,2	0.180	0.144	-0.06 ± 0.05	0.06 ± 0.04	0.07 ± 0.06	-0.06 ± 0.10
5,3	0.018	0.209	-0.12 ± 0.05	0.09 ± 0.05	-0.05 ± 0.09	-0.03 ± 0.06
5,4	0.037	0.011	-0.06 ± 0.05	-0.11 ± 0.04	-0.13 ± 0.05	-0.08 ± 0.04
5,5	0.122	0.077	0.07 ± 0.02	0.10 ± 0.03	-0.11 ± 0.03	0.10 ± 0.03
$W(5)$	0.13		0.07 ± 0.02			
$\theta°$	-27.4		-30.5 ± 1			
$\varphi°$	21.0		5.8 ± 4			
$\lambda°$	-17.4		-35.5 ± 5			

*This value reflects the offset of the LRO data from the LRO reference radius.

Table S6. Gravity spherical harmonic coefficients calculated outside SPA and 12 large basins, fit up to degree 5, in the present Earth-facing frame and principal frame. Coefficients derived from global data in the present frame, and gravity coefficients rotated into topography's principal frame are also shown. $W(n)$ is the power for degree n (eq. S3) (equal in principal and present frames). The angles for rotation of gravity into its principal frame using data outside SPA and large basins, are shown at the bottom. Uncertainties are derived from Monte Carlo analysis. Coefficients used in analysis in main text are highlighted.

	Global data, present frame		**Fit outside basins, present frame** $\times 10^{-5}$ ($\pm 1\sigma$)		**Fit outside basins, principal frame** $\times 10^{-5}$ ($\pm 1\sigma$)		**Fit outside basins, topography principal frame** $\times 10^{-5}$ ($\pm 1\sigma$)	
Deg., Order	***C***	***S***	***C***	***S***	***C***	***S***	***C***	***S***
0,0			0.7 ± 0.3		0.2 ± 0.3		0.7 ± 0.3	
1,0			1.3 ± 0.4		1.2 ± 0.4		1.4 ± 0.3	
1,1			-1.5 ± 0.4	-0.5 ± 0.1	-1.5 ± 0.4	-0.5 ± 0.1	-1.4 ± 0.4	-0.6 ± 0.3
$W(1)$			$0.4 \pm 0.1 \times 10^{-9}$					
2,0	-9.09×10^{-5}		-8.4 ± 0.3		-8.5 ± 0.3		-4.3 ± 0.7	
2,1			0.7 ± 0.5	0.5 ± 0.2			3.7 ± 0.5	-5.9 ± 0.3
2,2	3.47×10^{-5}		3.4 ± 0.2	0.3 ± 0.1	3.4 ± 0.2		3.9 ± 0.6	-0.9 ± 0.3
$W(2)$	9.5×10^{-9}		$8.4 \pm 0.4 \times 10^{-9}$					
3,0	3.20×10^{-6}		0.0 ± 0.2		0.3 ± 0.2		-0.1 ± 0.5	
3,1	2.64×10^{-5}	5.46×10^{-6}	1.7 ± 0.5	0.7 ± 0.2	1.6 ± 0.5	0.6 ± 0.2	1.4 ± 0.6	0.7 ± 0.3
3,2	1.42×10^{-5}	4.88×10^{-6}	0.5 ± 0.4	0.1 ± 0.2	0.6 ± 0.3	0.3 ± 0.2	0.5 ± 0.2	1.1 ± 0.1
3,3	1.23×10^{-5}	-1.77×10^{-6}	1.0 ± 0.2	0.0 ± 0.1	1.0 ± 0.2	-0.1 ± 0.2	-0.4 ± 0.2	-0.6 ± 0.1
$W(3)$	0.1×10^{-9}		$0.4 \pm 0.1 \times 10^{-9}$					
4,0	3.24×10^{-6}		0.4 ± 0.2		0.4 ± 0.2		0.4 ± 0.3	
4,1	-6.01×10^{-6}	1.66×10^{-6}	0.3 ± 0.3	0.2 ± 0.1	0.3 ± 0.3	0.2 ± 0.2	0.5 ± 0.5	0.0 ± 0.2
4,2	-7.12×10^{-6}	-6.78×10^{-6}	-0.3 ± 0.3	-0.3 ± 0.2	-0.2 ± 0.4	-0.1 ± 0.2	-0.7 ± 0.3	-0.5 ± 0.4
4,3	-1.35×10^{-6}	-1.34×10^{-5}	-0.1 ± 0.2	-1.2 ± 0.2	-0.3 ± 0.2	-1.2 ± 0.2	-0.3 ± 0.1	-0.2 ± 0.2
4,4	-6.00×10^{-6}	3.93×10^{-6}	-0.3 ± 0.1	0.4 ± 0.1	-0.2 ± 0.1	0.3 ± 0.1	0.6 ± 0.2	-0.6 ± 0.2
$W(4)$	0.4×10^{-9}		$0.2 \pm 0.3 \times 10^{-9}$					
5,0	-2.24×10^{-7}		0.0 ± 0.2		0.1 ± 0.1		0.3 ± 0.3	
5,1	-1.01×10^{-6}	-4.12×10^{-6}	0.2 ± 0.2	-0.5 ± 0.1	0.2 ± 0.2	-0.6 ± 0.1	-0.9 ± 0.3	0.2 ± 0.2
5,2	4.40×10^{-6}	1.06×10^{-6}	-0.3 ± 0.2	0.1 ± 0.2	-0.2 ± 0.2	-0.7 ± 0.2	-0.2 ± 0.3	-0.1 ± 0.4
5,3	4.66×10^{-7}	8.70×10^{-6}	-0.7 ± 0.2	0.8 ± 0.2	-0.6 ± 0.2	0.8 ± 0.2	-0.1 ± 0.2	0.0 ± 0.4
5,4	2.75×10^{-6}	6.76×10^{-8}	-0.3 ± 0.2	-0.0 ± 0.2	-0.4 ± 0.2	0.1 ± 0.1	-0.6 ± 0.2	-0.1 ± 0.1
5,5	3.11×10^{-6}	-2.76×10^{-6}	0.3 ± 0.1	-0.4 ± 0.1	0.1 ± 0.1	-0.5 ± 0.1	-0.6 ± 0.1	-0.3 ± 0.1
$W(5)$	0.1×10^{-9}		$0.2 \pm 0.3 \times 10^{-9}$					
$\theta°$			-2.6 ± 1				-30.5*	
$\varphi°$			-2.3 ± 2				5.8*	
$\lambda°$			-2.3 ± 1				-35.5*	

*From topography principal frame calculation (Table S5).

Table S7. Topography and gravity principal axis locations with and without large basins (Latitude°, Longitude° E) ($\pm 1\sigma$).

	Largest axis (minimum moment axis)	**Intermediate axis**	**Smallest axis (largest moment axis)**
Global topography data	(21.0°, 207.4°)	(-16.1°, 290.9°)	(63.1°, 346.3°)
Topography fit outside basins, degrees 0-5*	(5.9° ± 4°, 210.4° ± 1°)	(-35.1° ± 5°, 296.4° ± 4°)	(54.4° ± 5°, 308.6 ± 6°)
Global gravity data	(0°, 180°)	(0°, 270°)	(90°, 0°)
Gravity fit outside basins, degrees 0-5*	(-4.8° ± 2°, 182.0° ± 1°)	(-1.8° ± 1°, 272.1 ± 1°)	(84.9° ± 2°, 202.9° ± 35°)

*Used in main text.

Table S8. Compensated and uncompensated degree-2 topography spherical harmonic coefficients calculated using the basin-filling method. Corrections and uncertainties are obtained using calculations with synthetic maps (Section S3).

	Compensated topography	**Uncompensated topography**	**Compensated topography corrected, with 1σ uncertainties**	**Uncompensated topography corrected, with 1σ uncertainties**
10% larger outer basin diameter				
$C_{2,0}$	-0.47	-0.08	-0.5 ± 0.2	-0.10 ± 0.01
$C_{2,2}$	0.35	0.11	0.39 ± 0.08	0.12 ± 0.03
$C_{2,0}/C_{2,2}$	-1.35	-0.7	-1.4 ± 0.6	-0.8 ± 0.2
20% larger outer basin diameter				
$C_{2,0}$	-0.49	-0.08	-0.6 ± 0.2	-0.10 ± 0.01
$C_{2,2}$	0.34	0.11	0.39 ± 0.08	0.12 ± 0.03
$C_{2,0}/C_{2,2}$	-1.40	-0.7	-1.5 ± 0.6	-0.8 ± 0.2

Table S9. C_{20} and C_{22} topography and gravity coefficients ($\pm$ 1σ) calculated outside of the Moon's large basins, in topography's principal frame (Figs. 2d and 2e). The theoretical compensated and uncompensated topography required to produce gravity observations is shown in the top half of the table. The linear combination of compensated and uncompensated topography that matches both observed gravity and topography is shown in the lower half of the table (see Fig. S9). Compensated and uncompensated topography harmonics are associated with crustal thickness variations and a fossil bulge, respectively.

	Observed gravity with basins removed (Fig. 2e)	Compensated topography*	Uncompensated topography*	Observed topography with basins removed (Fig. 2d)
		Required to produce gravity:		
$C_{2,0}$	$-4.3 \pm 0.7 \times 10^{-5}$	-1.8 ± 0.3 km	-0.17 ± 0.03 km	-0.65 ± 0.05 km
$C_{2,2}$	$3.9 \pm 0.6 \times 10^{-5}$	1.6 ± 0.2 km	0.15 ± 0.02 km	0.51 ± 0.05 km
		Linear combination to match topography and gravity:*		
$C_{2,0}$		-0.53 ± 0.07 km	-0.11 ± 0.04 km	
$C_{2,2}$		0.40 ± 0.06 km	0.11 ± 0.03 km	
$C_{2,0}/C_{2,2}$		-1.3 ± 0.2	-1.0 ± 0.3	

*Assumes crustal density 2550 kg/m^3, mantle density 3200 kg/m^3, mean lunar density 3340 kg/m^3, and mean crustal thickness 40 km[19]. Some values may not sum due to rounding.

Table S10. C_{20} and C_{22} topography and gravity coefficients in topography's principal frame, using *global* data (compare with Table 1 and Table S9). The compensated and uncompensated topography required to produce gravity observations is shown in the top half of the table. The linear combination of compensated and uncompensated topography that matches both observed gravity and topography is shown in the lower half of the table. Compensated and uncompensated topography are associated with crustal thickness variations and a fossil bulge, respectively.

	Observed global gravity	Compensated topography*	Uncompensated topography*	Observed global topography
		Required to produce gravity:		
$C_{2,0}$	-5.74×10^{-5}	-2.4 km	-0.22 km	-1.00 km
$C_{2,2}$	1.66×10^{-5}	0.7 km	0.06 km	0.45 km
		Linear combination to match topography and gravity*:		
$C_{2,0}$		-0.86 km	-0.14 km	
$C_{2,2}$		0.43 km	0.02 km	
$C_{2,0}/C_{2,2}$		-2.0	-6.1	

*Assumes crustal density 2550 kg/m^3, mantle density 3200 kg/m^3, mean lunar density 3340 kg/m^3, and mean crustal thickness 40 km[19]. Uncertainties are small and not shown, since these globally-determined harmonics are well known.

Table S11. Crustal thickness spherical harmonic coefficients calculated outside SPA and 12 large basins, fit up to degree 5, in the present Earth-facing frame and principal frame. Coefficients derived from global data in the present frame are also shown. $W(n)$ is the power for degree n (eq. S3) (km^2) (equal in principal and present frames). The angles for rotation of crustal thickness into its principal frame using global data, and using data outside SPA and large basins, are shown at the bottom. The ratio $C_{2,0}/C_{2,2}$ in the crustal thickness principal frame is also shown. Uncertainties are derived from Monte Carlo analysis.

	Global data, present frame, km		**Fit outside basins, present frame, km (± 1σ)**		**Fit outside basins, principal frame, km (± 1σ)**	
Degree, Order	***C***	***S***	***C***	***S***	***C***	***S***
0,0	0*		2.53 ± 0.65		2.52 ± 0.66	
1,0	0.65	0.00	-1.17 ± 0.80		-2.16 ± 0.40	
1,1	-5.01	-1.90	-5.90 ± 0.66	-1.98 ± 0.21	-5.91 ± 0.80	-0.20 ± 0.43
$W(1)$	29.1		40 ± 6			
2,0	-2.47	0.00	-1.48 ± 0.51		-2.70 ± 0.39	
2,1	-3.79	-0.07	-0.83 ± 0.98	0.72 ± 0.25		
2,2	0.04	2.06	1.19 ± 0.41	2.93 ± 0.22	2.50 ± 0.23	
$W(2)$	24.7		13 ± 2			
3,0	0.45	0.00	-0.24 ± 0.32		-0.52 ± 0.80	
3,1	2.22	0.08	0.13 ± 0.84	-0.73 ± 0.24	1.03 ± 0.54	1.04 ± 0.31
3,2	1.87	0.99	0.91 ± 0.67	0.21 ± 0.31	1.14 ± 0.48	-0.40 ± 0.32
3,3	1.92	-0.18	1.47 ± 0.26	-0.47 ± 0.21	0.20 ± 0.45	0.06 ± 0.38
$W(3)$	13.3		4 ± 1			
4,0	1.01	0.00	0.60 ± 0.34		0.01 ± 0.38	
4,1	-0.90	-0.41	-0.07 ± 0.50	-0.20 ± 0.22	0.21 ± 0.51	-0.40 ± 0.43
4,2	-1.49	-0.44	0.24 ± 0.64	0.13 ± 0.33	-1.08 ± 0.37	0.12 ± 0.63
4,3	-0.96	-1.02	-0.01 ± 0.40	-0.41 ± 0.31	0.46 ± 0.35	0.34 ± 0.31
4,4	-0.88	0.74	-0.54 ± 0.21	0.99 ± 0.16	0.44 ± 0.41	-0.14 ± 0.27
$W(4)$	7.7		1.9 ± 0.5			
5,0	-0.65	0.00	-0.34 ± 0.32		0.15 ± 0.41	
5,1	0.27	-0.07	-0.38 ± 0.36	0.04 ± 0.18	0.13 ± 0.40	0.35 ± 0.39
5,2	1.00	0.77	0.01 ± 0.45	0.08 ± 0.29	0.60 ± 0.33	-0.04 ± 0.38
5,3	-0.18	0.92	-0.49 ± 0.40	0.11 ± 0.34	0.34 ± 0.43	-0.11 ± 0.29
5,4	0.05	-0.02	-0.05 ± 0.31	-0.70 ± 0.26	-0.12 ± 0.49	-0.30 ± 0.28
5,5	0.61	-0.41	0.41 ± 0.15	-0.41 ± 0.19	-0.53 ± 0.27	-0.56 ± 0.35
$W(5)$	3.5		1.3 ± 0.5			
$\theta°$	-32.3		-33.4 ± 2			
$\varphi°$	23.2		2.9 ± 8			
$\lambda°$	-24.2		-52.8 ± 14			
$C_{2,0}/C_{2,2}$					-1.1 ± 0.2	

*The mean crustal thickness is 43 km, but it was subtracted before using the data.

Table S12. Comparison of degree-2 and degree-4 coefficients for topography, gravity, and crustal thickness, calculated outside of large basins (taken from Tables S5, S6, and S11). The degree-4 coefficient that is largest in tidal heating models, $C_{4,4}$, is highlighted. Crustal thickness is shown both in topography's principal frame, and its own principal frame. The predicted value of $C_{2,0}/C_{4,4}$ is approximately -0.45 when tidal heating is important.

	Topography, topography principal frame, km (± 1σ)		**Gravity, topography principal frame (× 10^{-4}) (± 1σ)**		**Crustal thickness, topography principal frame, km (± 1σ)**		**Crustal thickness, crustal thickness principal frame, km (± 1σ)**	
Degree, Order	***C***	***S***	***C***	***S***	***C***	***S***	***C***	***S***
2,0	-0.65 ± 0.05		-4.3 ± 0.7		-2.54 ± 0.37		-2.70 ± 0.39	
2,1			3.7 ± 0.5	-5.9 ± 0.3	0.05 ± 0.04	0.62 ± 0.10		
2,2	0.51 ± 0.05		3.9 ± 0.6	-0.9 ± 0.3	2.55 ± 0.23	0.34 ± 0.05	2.50 ± 0.23	
4,0	0.04 ± 0.07		0.4 ± 0.3		-0.03 ± 0.05		0.01 ± 0.38	
4,1	0.05 ± 0.13	0.05 ± 0.05	0.5 ± 0.5	0.0 ± 0.2	0.13 ± 0.30	0.29 ± 0.23	0.21 ± 0.51	-0.40 ± 0.43
4,2	-0.22 ± 0.06	-0.15 ± 0.09	-0.7 ± 0.3	-0.5 ± 0.4	-0.78 ± 0.21	-0.34 ± 0.20	-1.08 ± 0.37	0.12 ± 0.63
4,3	-0.05 ± 0.03	0.05 ± 0.04	-0.3 ± 0.3	-0.2 ± 0.2	0.21 ± 0.14	0.73 ± 0.27	0.46 ± 0.35	0.34 ± 0.31
4,4	0.11 ± 0.05	-0.11 ± 0.03	0.6 ± 0.2	-0.6 ± 0.2	0.72 ± 0.34	-0.13 ± 0.04	0.44 ± 0.41	-0.14 ± 0.27
$C_{2,0}/C_{4,4}$					-0.28 ± 0.14			

Table S13. Summary of tidal heating calculations (see Section S8).

Case #	Eccentricity	Basal crustal heat flux (mW/m^2)	Basal crust temperature (°C)	Mean thickness (km)	$C_{2,0}$ (km)	$C_{2,2}$ (km)	$C_{2,0}/C_{2,2}$	Tidal heat flux (mW/m^2)
1	0.02	20	1125	101.3	-0.23	0.67	-0.34	0.7
2	0.02	20	1150	97.8	-3.80	1.88	-2.02	2.0
3	0.02	20	1175	87.0	-10.01	4.61	-2.17	5.9
4	0.02	20	1200	68.6	-13.98	8.26	-1.69	15.5
5	0.02	20	1225	48.4	-12.36	9.69	-1.28	34.4
6	0.02	20	1250	32.6	-8.51	7.60	-1.12	63.6
7	0.02	20	1275	23.6	-5.05	4.73	-1.07	94.3
8	0.02	20	1300	20.0	-3.20	2.83	-1.13	115.5
9	0.02	20	1325	19.2	-2.48	2.06	-1.20	127.0
10	0.02	20	1350	19.6	-2.17	1.76	-1.24	133.1
11	0.02	20	1375	20.6	-2.02	1.62	-1.25	136.7
12	0.02	20	1400	21.9	-1.94	1.53	-1.27	139.0
13	0.02	20	1425	23.6	-1.89	1.48	-1.28	140.7
14	0.02	20	1450	25.4	-1.81	1.44	-1.26	141.8
15	0.02	30	1125	68.7	0.60	0.29	3.03	0.4
16	0.02	30	1150	68.4	-0.55	0.57	-0.95	1.3
17	0.02	30	1175	65.3	-3.32	1.54	-2.20	3.7
18	0.02	30	1200	57.2	-7.48	3.53	-2.12	10.5
19	0.02	30	1225	44.7	-9.43	5.88	-1.60	26.1
20	0.02	30	1250	32.0	-7.87	6.36	-1.24	53.4
21	0.02	30	1275	23.3	-4.98	4.61	-1.08	84.8
22	0.02	30	1300	19.5	-3.14	2.78	-1.13	107.4
23	0.02	30	1325	18.5	-2.38	1.99	-1.20	119.6
24	0.02	30	1350	18.6	-2.08	1.67	-1.25	126.0
25	0.02	30	1375	19.3	-1.94	1.54	-1.26	130.0
26	0.02	30	1400	20.2	-1.86	1.45	-1.28	132.7
27	0.02	30	1425	21.4	-1.79	1.41	-1.27	134.7
28	0.02	30	1450	22.6	-1.76	1.37	-1.29	136.6
29	0.02	40	1125	51.8	0.65	0.08	7.8	0.3
30	0.02	40	1150	52.2	0.16	0.24	0.66	0.9
31	0.02	40	1175	51.3	-1.13	0.67	-1.69	2.7
32	0.02	40	1200	47.6	-3.78	1.68	-2.25	7.6
33	0.02	40	1225	40.1	-6.55	3.40	-1.93	20.1
34	0.02	40	1250	30.7	-6.89	4.61	-1.49	44.5
35	0.02	40	1275	22.8	-4.75	4.21	-1.13	76.1
36	0.02	40	1300	19.0	-3.03	2.67	-1.14	99.7
37	0.02	40	1325	17.9	-2.28	1.87	-1.22	112.6
38*	0.02	40	1350	17.8	-1.98	1.57	-1.26	119.6
39	0.02	40	1375	18.3	-1.84	1.44	-1.28	123.7
40	0.02	40	1400	19.0	-1.76	1.37	-1.29	126.7
41	0.02	40	1425	19.8	-1.70	1.32	-1.28	129.0
42	0.02	40	1450	20.8	-1.66	1.29	-1.29	131.0
43	0.025	20	1125	96.7	-2.99	1.60	-1.87	1.7

44	0.025	20	1150	86.9	-9.11	4.13	-2.2	5.2
45	0.025	20	1175	68.8	-13.6	7.92	-1.72	14.5
46	0.025	20	1200	48.1	-12.35	9.55	-1.29	33.7
47	0.025	20	1225	31.6	-8.58	7.59	-1.13	65.5
48	0.025	20	1250	21.5	-5.13	4.80	-1.07	105.1
49	0.025	20	1275	16.9	-3.07	2.78	-1.10	137.7
50	0.025	20	1300	15.6	-2.18	1.86	-1.17	156.3
51	0.025	20	1325	15.7	-1.83	1.50	-1.22	166.0
52	0.025	20	1350	16.5	-1.68	1.35	-1.25	171.2
53	0.025	20	1375	17.6	-1.60	1.26	-1.27	174.4
54	0.025	20	1400	19.1	-1.55	1.22	-1.28	176.4
55	0.025	20	1425	20.9	-1.49	1.18	-1.26	177.6
56	0.025	30	1125	67.2	-0.27	0.48	-0.57	1.1
57	0.025	30	1150	64.6	-2.82	1.36	-2.08	3.3
58	0.025	30	1175	56.9	-7.02	3.27	-2.15	9.6
59	0.025	30	1200	44.4	-9.30	5.71	-1.63	25.2
60	0.025	30	1225	31.1	-7.94	6.35	-1.25	54.6
61	0.025	30	1250	21.5	-5.15	4.73	-1.09	94.5
62	0.025	30	1275	16.7	-3.06	2.79	-1.10	128.4
63	0.025	30	1300	15.2	-2.14	1.82	-1.18	148.2
64	0.025	30	1325	15.1	-1.79	1.45	-1.23	158.5
65	0.025	30	1350	15.6	-1.63	1.30	-1.25	154.3
66	0.025	30	1375	16.5	-1.55	1.22	-1.27	167.9
67	0.025	30	1400	17.5	-1.48	1.17	-1.26	170.3
68	0.025	30	1425	18.7	-1.45	1.14	-1.27	172.5
69	0.025	30	1450	20.1	-1.40	1.11	-1.26	174.0
70	0.025	40	1125	51.2	0.28	0.21	1.35	0.8
71	0.025	40	1150	50.5	-0.89	0.59	-1.51	2.4
72	0.025	40	1175	47.1	-3.45	1.54	-2.24	7.0
73	0.025	40	1200	39.7	-6.37	3.26	-1.96	19.3
74	0.025	40	1225	29.8	-6.82	4.73	-1.44	45.6
75	0.025	40	1250	21.2	-4.98	4.34	-1.15	84.8
76	0.025	40	1275	16.5	-3.01	2.76	-1.09	119.9
77	0.025	40	1300	14.8	-2.08	1.76	-1.19	140.8
78	0.025	40	1325	14.6	-1.72	1.39	-1.23	151.5
79	0.025	40	1350	15.0	-1.56	1.24	-1.26	157.6
80	0.025	40	1375	15.6	-1.49	1.17	-1.27	161.6
81	0.025	40	1400	16.4	-1.42	1.12	-1.27	164.3
82	0.025	40	1425	17.3	-1.40	1.09	-1.29	166.9
83	0.025	40	1450	18.3	-1.35	1.07	-1.27	168.8
84	0.03	20	1125	89.5	-6.94	3.12	-2.22	3.7
85	0.03	20	1150	73.3	-12.7	6.80	-1.87	11.1
86	0.03	20	1175	52.2	-12.88	9.42	-1.37	27.8
87	0.03	20	1200	34.1	-9.37	8.12	-1.15	57.8
88	0.03	20	1225	22.1	-5.83	5.35	-1.09	102.0
89	0.03	20	1325	13.5	-1.47	1.19	-1.23	204.0
90	0.03	20	1350	14.5	-1.36	1.10	-1.24	208.2
91	0.03	20	1375	15.7	-1.30	1.04	-1.25	210.8

92	0.03	20	1400	17.3	-1.27	1.01	-1.26	212.6
93	0.03	20	1425	19.0	-1.28	0.99	-1.30	214.3
94	0.03	30	1125	64.9	-1.77	0.99	-1.79	2.3
95	0.03	30	1150	58.7	-5.73	2.58	-2.22	7.2
96	0.03	30	1175	47.1	-8.98	5.09	-1.76	20.1
97	0.03	30	1200	33.3	-8.39	6.38	-1.31	47.1
98	0.03	30	1225	22.2	-5.82	5.17	-1.13	90.4
99	0.03	30	1325	13.0	-1.43	1.16	-1.24	196.4
100	0.03	30	1350	13.7	-1.33	1.07	-1.25	201.4
101	0.03	30	1375	14.6	-1.28	1.01	-1.26	204.8
102	0.03	30	1400	15.7	-1.25	0.98	-1.28	207.3
103	0.03	30	1425	17.0	-1.20	0.96	-1.25	208.8
104	0.03	30	1450	18.3	-1.21	0.93	-1.30	211.2
105	0.03	40	1125	50.2	-0.38	0.42	-0.91	1.7
106	0.03	40	1150	47.7	-2.53	1.17	-2.16	5.1
107	0.03	40	1175	41.3	-5.69	2.74	-2.08	15.1
108	0.03	40	1200	31.5	-6.93	4.48	-1.55	38.5
109	0.03	40	1225	22.0	-5.55	4.60	-1.20	79.9
110	0.03	40	1350	13.1	-1.30	1.03	-1.26	194.8
111	0.03	40	1375	13.8	-1.24	0.98	-1.26	198.6
112	0.03	40	1400	14.7	-1.21	0.94	-1.28	201.6
113	0.03	40	1425	15.6	-1.16	0.92	-1.26	203.7
114	0.03	40	1450	16.7	-1.16	0.90	-1.29	206.1

*Used in main text (Fig. 3 inset).

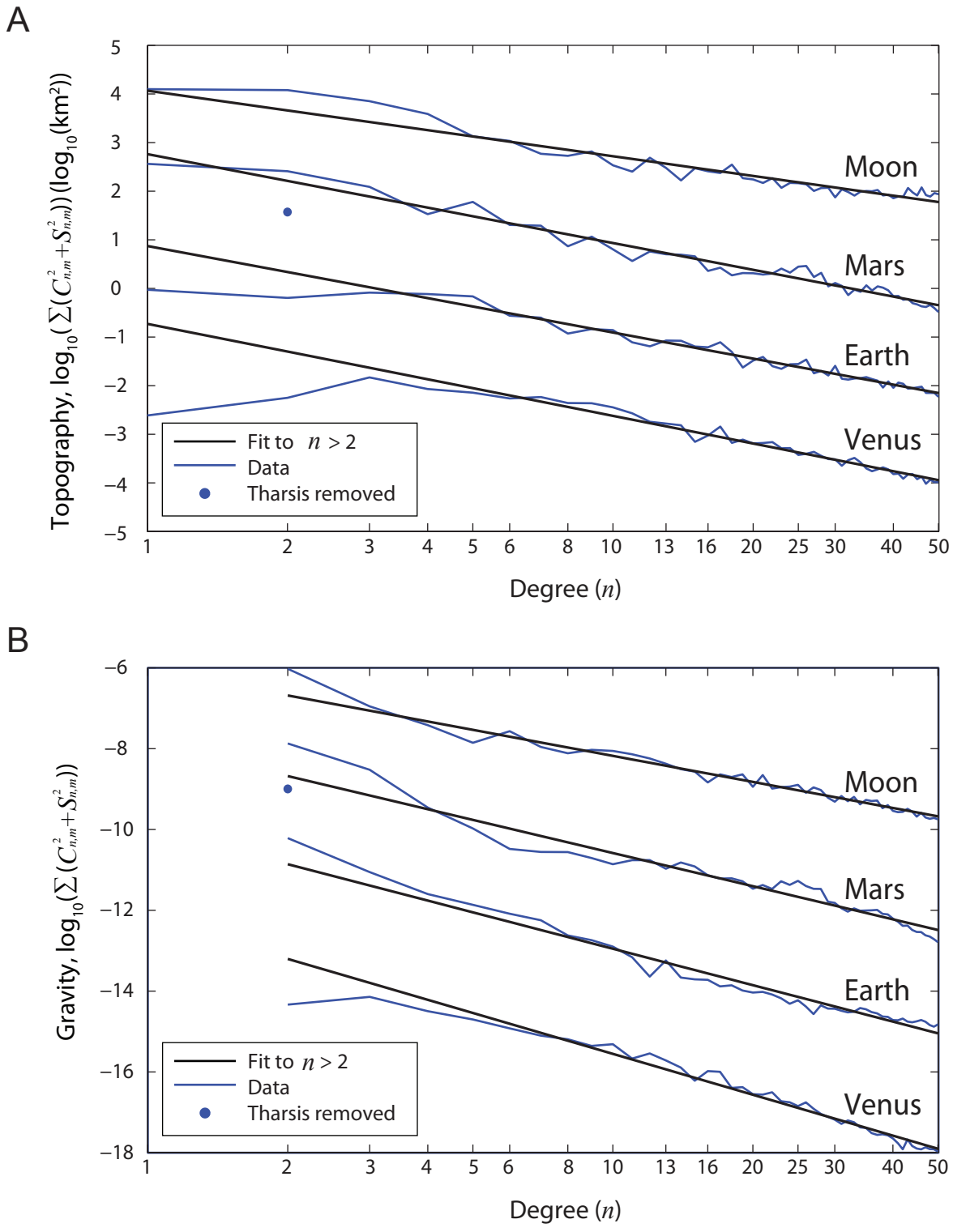

Figure S1. Power spectra of planetary topography (**A**), and gravity (**B**), offset for clarity. In logarithmic scale, lunar topography is offset by +4, and gravity by +2. Mars topography is offset by +2 and gravity by 0. Earth topography and gravity have not been offset. Venus topography is offset by -1 and gravity by -3. Tharsis has been removed by the methods discussed in Section S1.

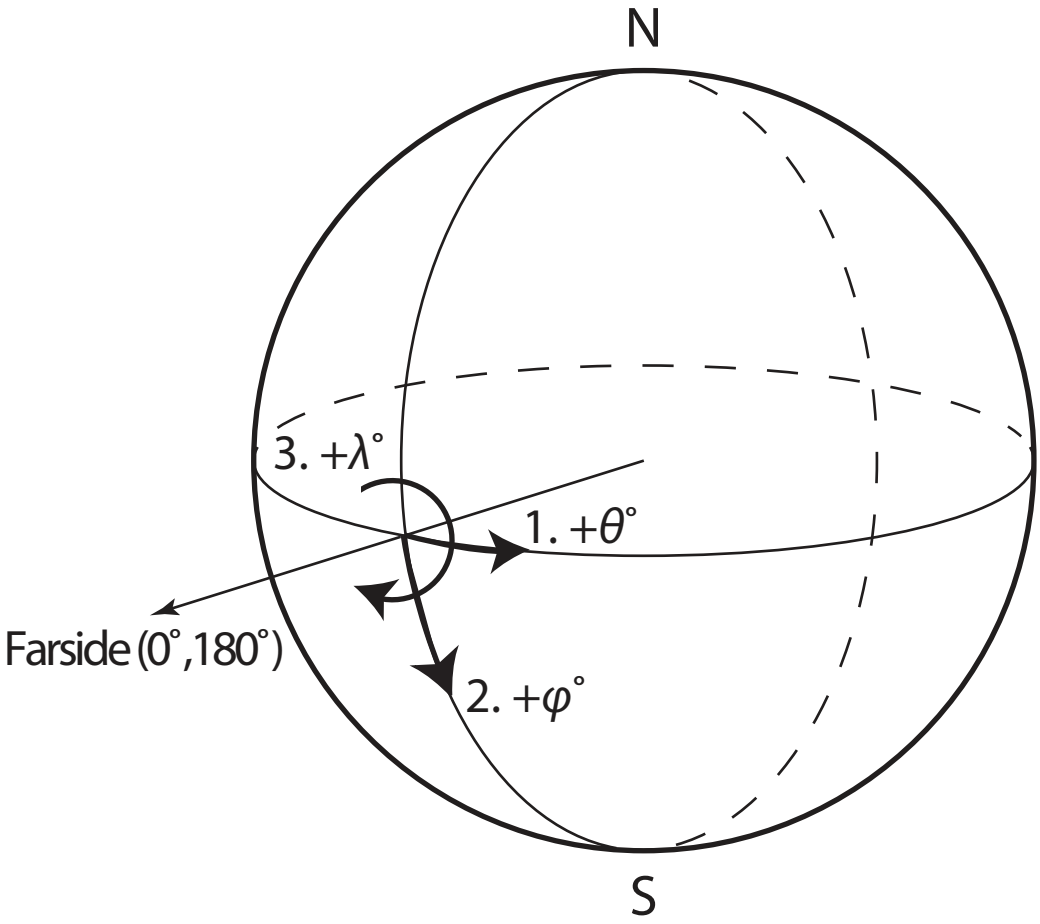

Figure S2. Definition of the rotation angles θ, φ, λ, and the order they are performed to rotate a set of data from the present reference frame into its principal reference frame.

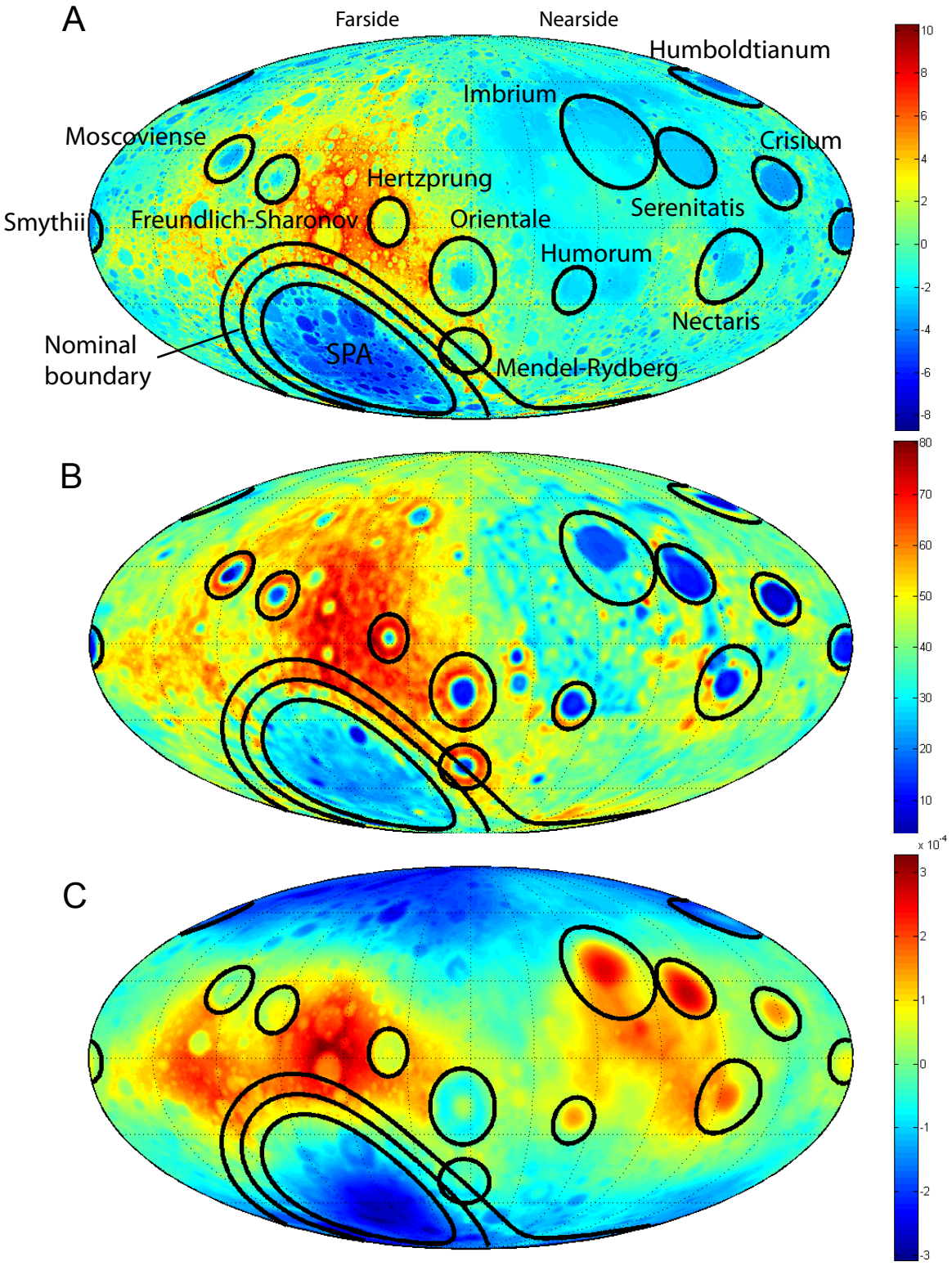

Figure S3. Map of large, well-defined lunar basins with strong signatures in topography, crustal thickness, or gravity. (**A**) Topography (km), (**B**) Crustal thickness (km), and (**C**) Gravity potential coefficient expansion (multiply by 2.823 x 10^6 m^2 s^{-2} to obtain surface potential). SPA boundaries are also shown for semi-axes 20% smaller, and 20% larger than nominal. See Table S3 for a list of basin diameters and locations.

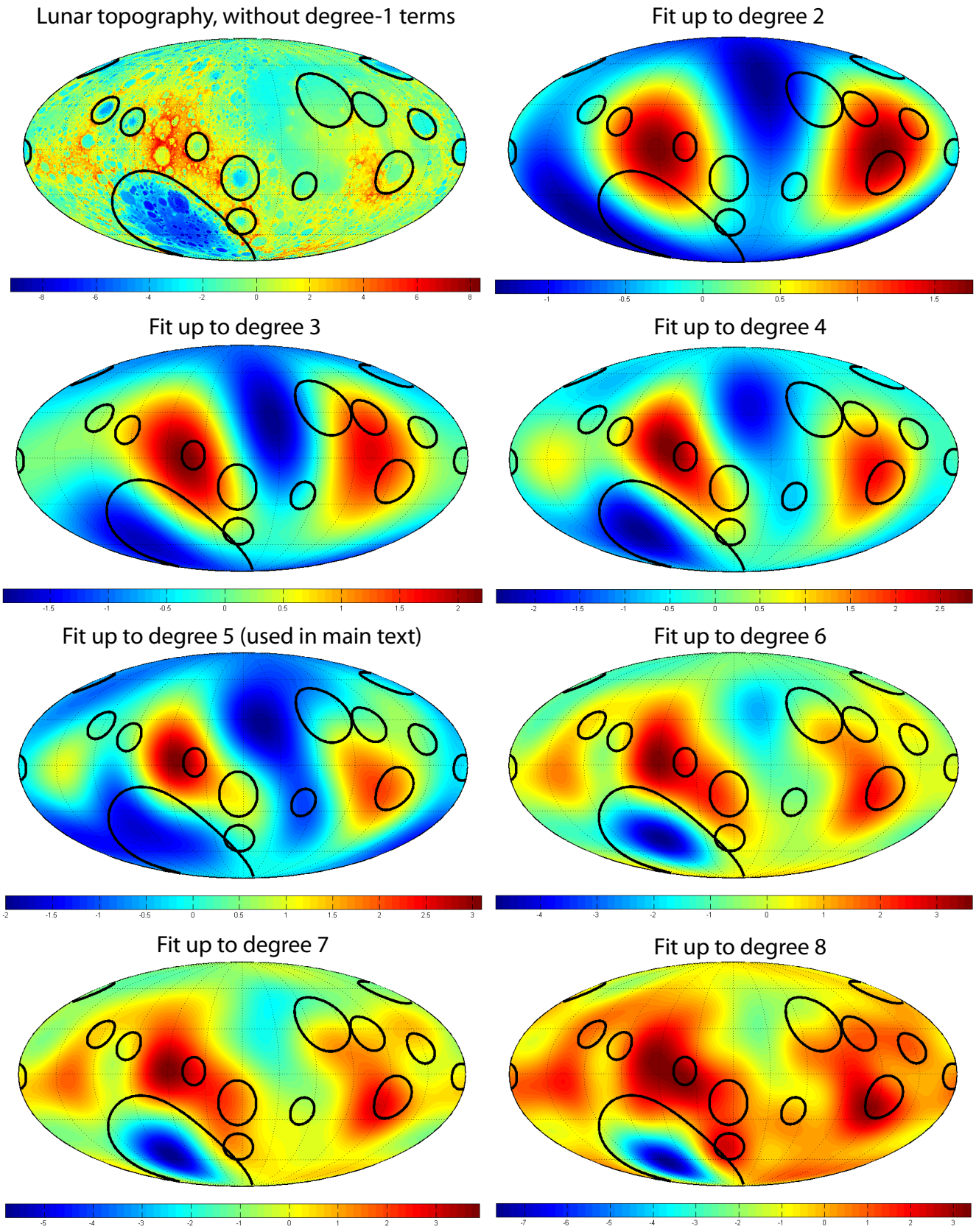

Figure S4. Expansions of best-fit lunar topography (km) outside of SPA and 12 other basins, from degree 2,up to the maximum degree shown (the degree-1 terms are calculated but not shown, since they would dominate the topography). Above degree 5, the hole at SPA starts to dominate the expansion. The fit up to degree 5 is used in the main text and for all conclusions (degree 4 yields similar results).

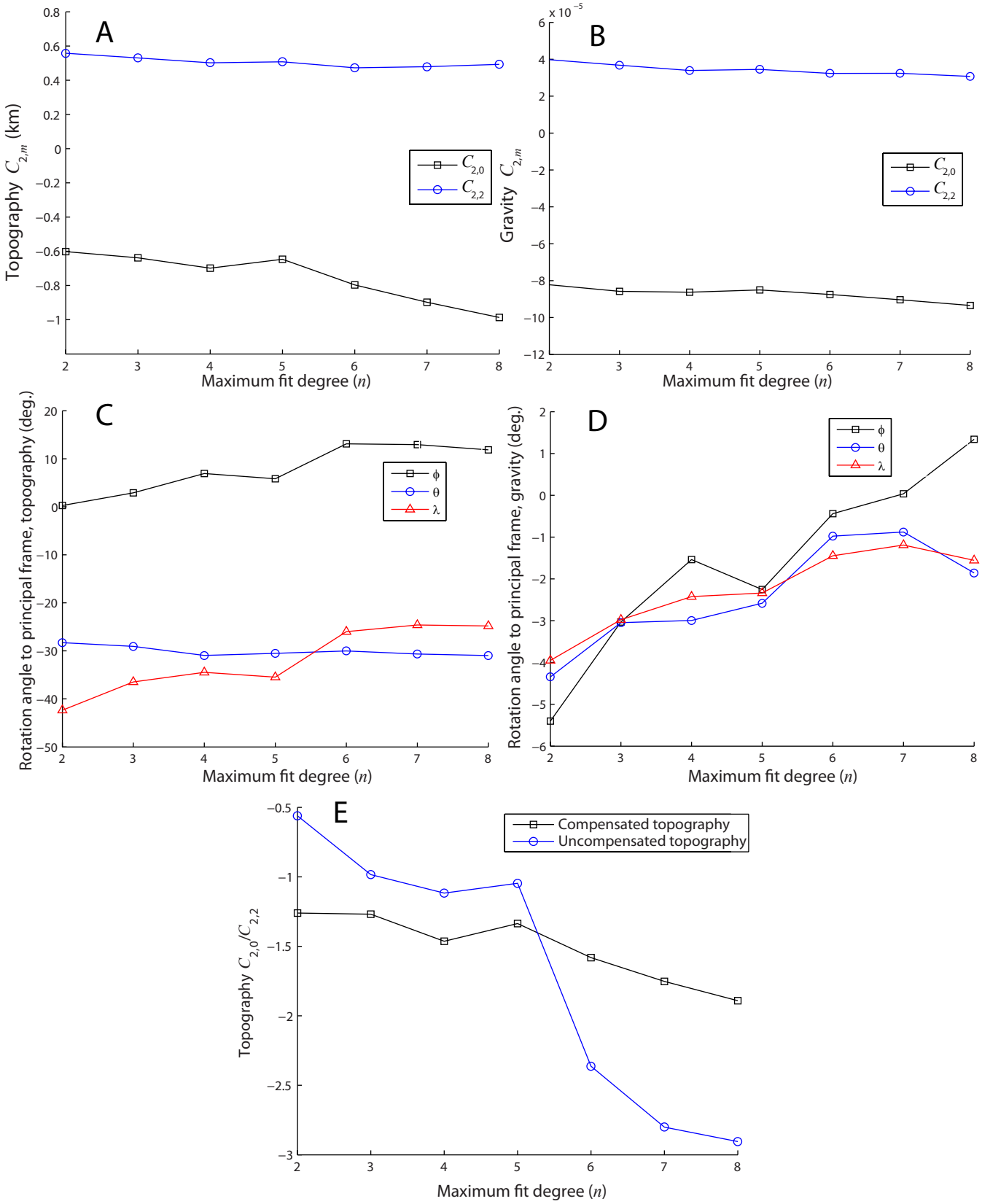

Figure S5. Effect of maximum fit degree on fit properties, for spherical harmonic fits to gravity and topography outside of large basins, up to the maximum degrees shown. (**A** and **B**) Degree-2 coefficients in the principal frame. (**C** and **D**) Principal frame rotation angles. (**E**) Ratio of $C_{2,0}/C_{2,2}$ for compensated and uncompensated topography. The expansion up to degree 5 is used in the main text and for all conclusions (see Section S2).

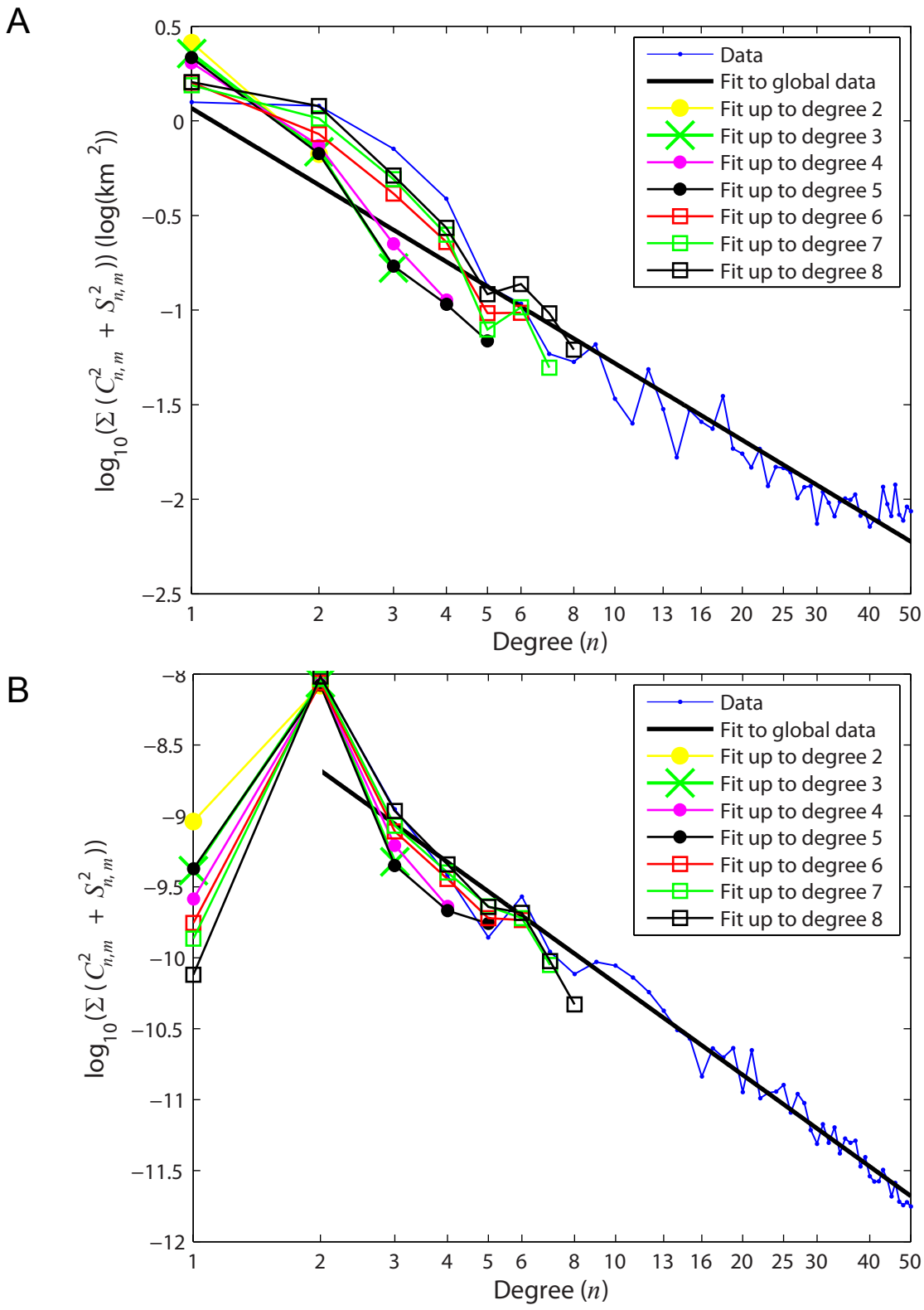

Figure S6. Power spectra for fits up to different maximum degrees for topograhy and gravity, outside large basins (global data also shown). (**A**) Topography. (**B**) Gravity potential. In both topography and gravity, the power increases at degrees 2 to 5 when the fit is performed above degree 5. See Section S2 and Fig. S4 and Fig. S5.

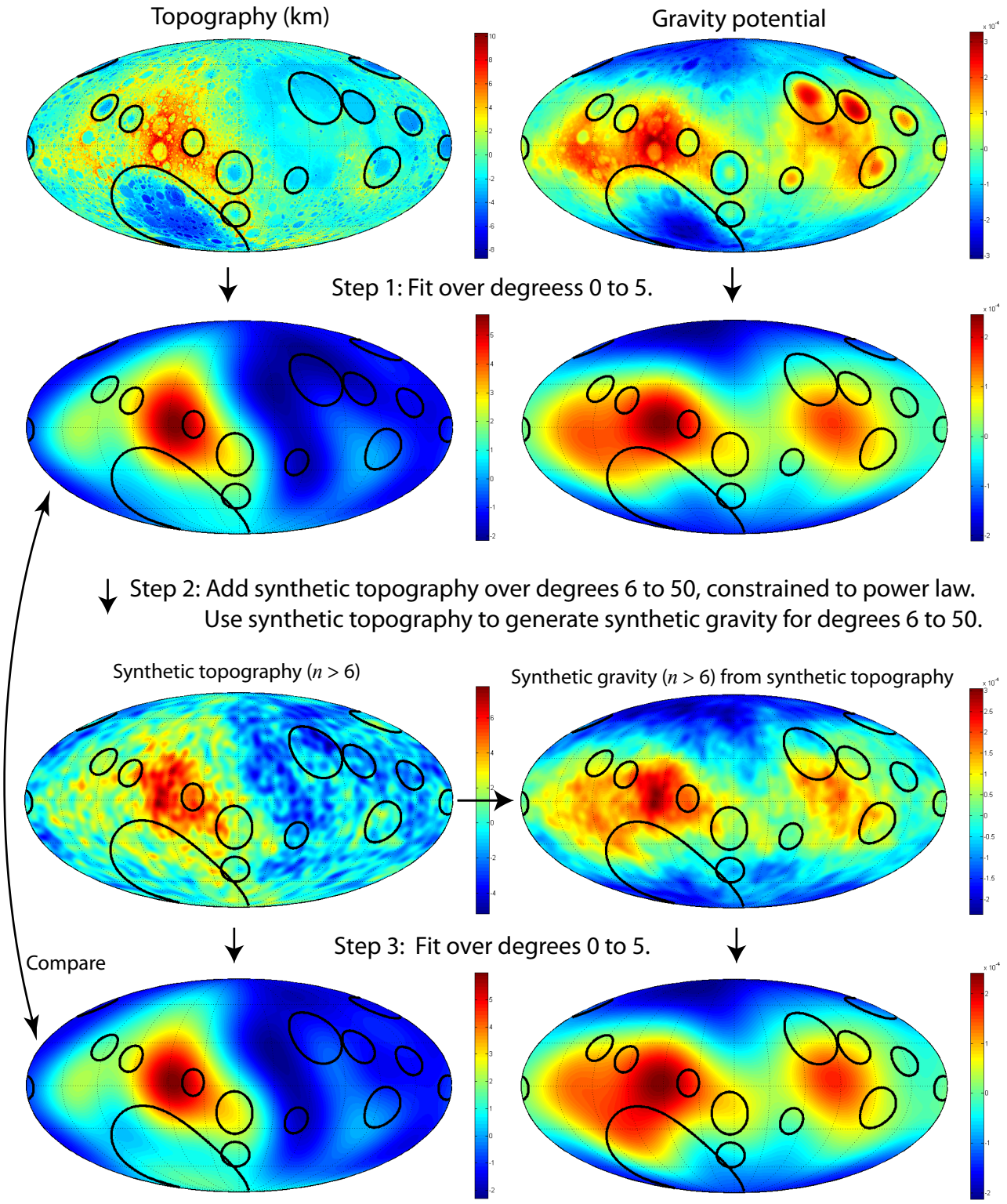

Figure S7. Method of determining uncertainty in fits to data outside of the Moon's large basins. For Step 2, the topography power-law coefficients are given in Table S1. An empircal relationship between topography and gravity is used to generate synthetic gravity. In the gravity figures, multiply by 2.823 x 10^6 m^2 s^{-2} to obtain surface potential. See Section S2.

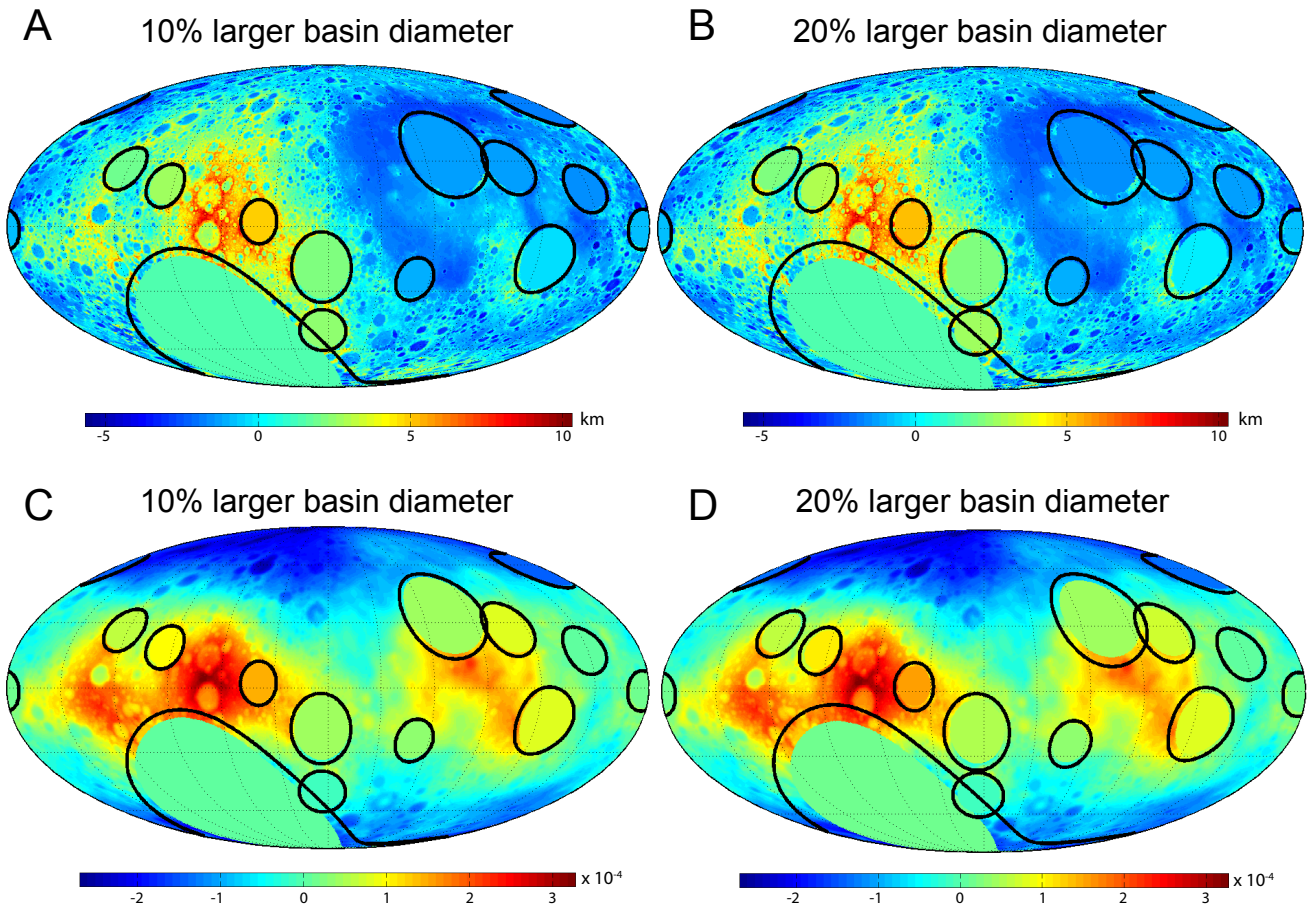

Figure S8. Topography and gravity with SPA and the next 12 largest basins filled in with the local mean topography or gravity. (**A and B**) Topography, using the mean of the area between the basin diamater and a diameter 10% and 20% larger. (**C and D**) Gravity, using the mean of the area between the basin diamater and a diameter 10% and 20% larger.

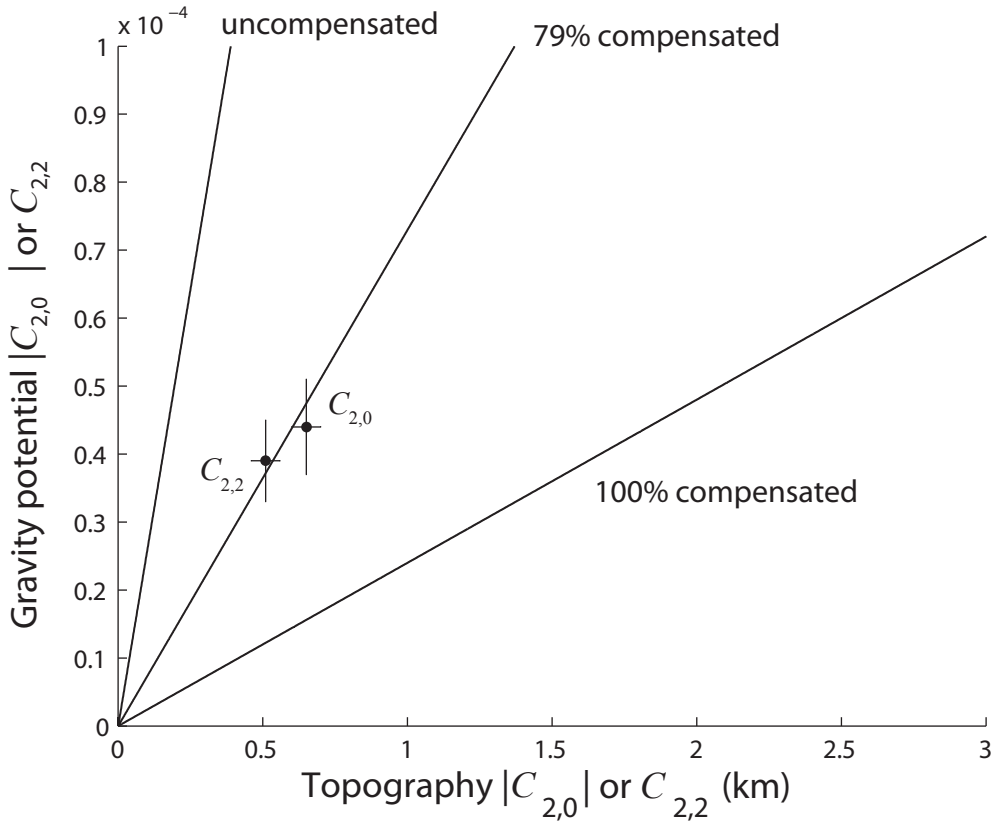

Figure S9. Gravity vs. topography for fully compensated or fully uncompesnated terrain. The degree-2 coefficients outside of large basins are shown (± 1σ). The topography is effectively ≈80% compensated for both coefficients.

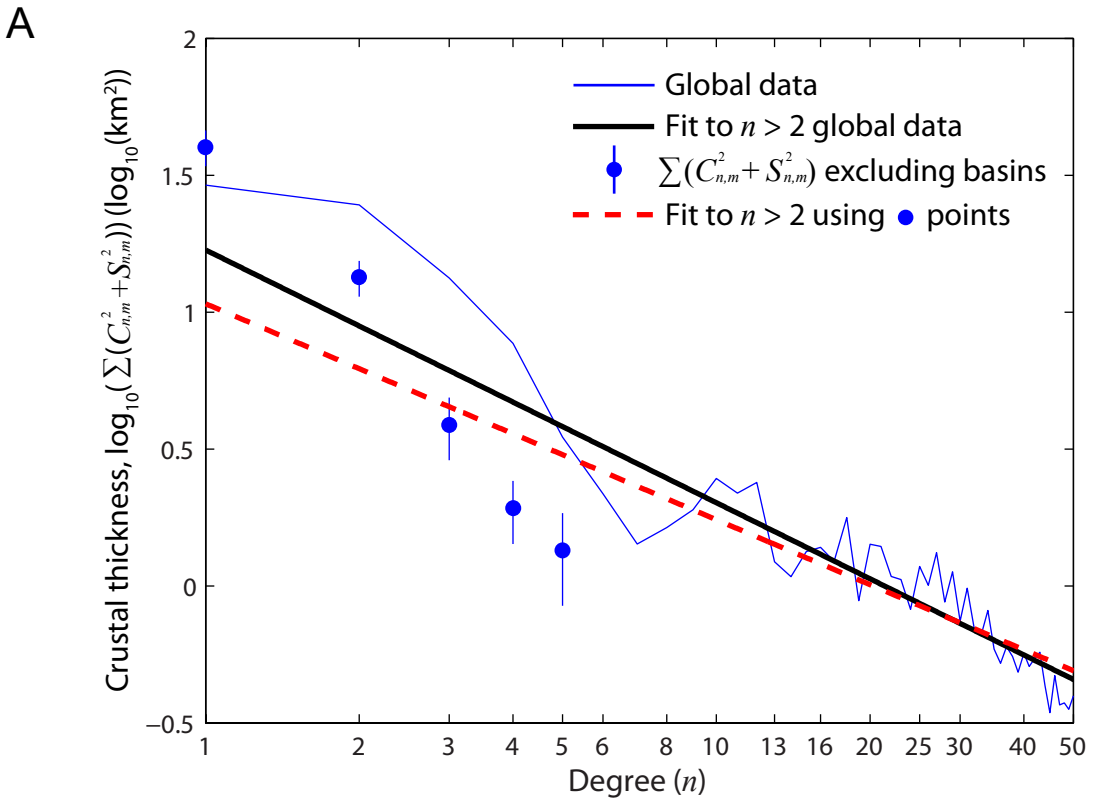

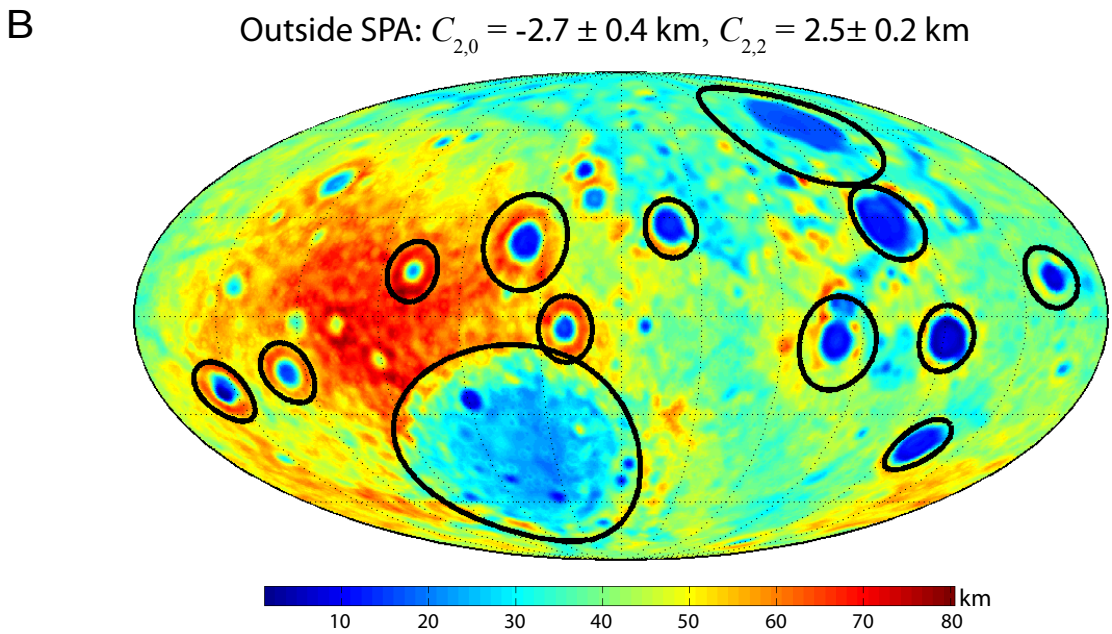

Figure S10. (**A**) Lunar crustal thickness power spectrum with best-fit power laws, analogous to Fig 1. (**B**) Lunar crustal thickness rotated to its principal frame, calculated outside the basins shown.

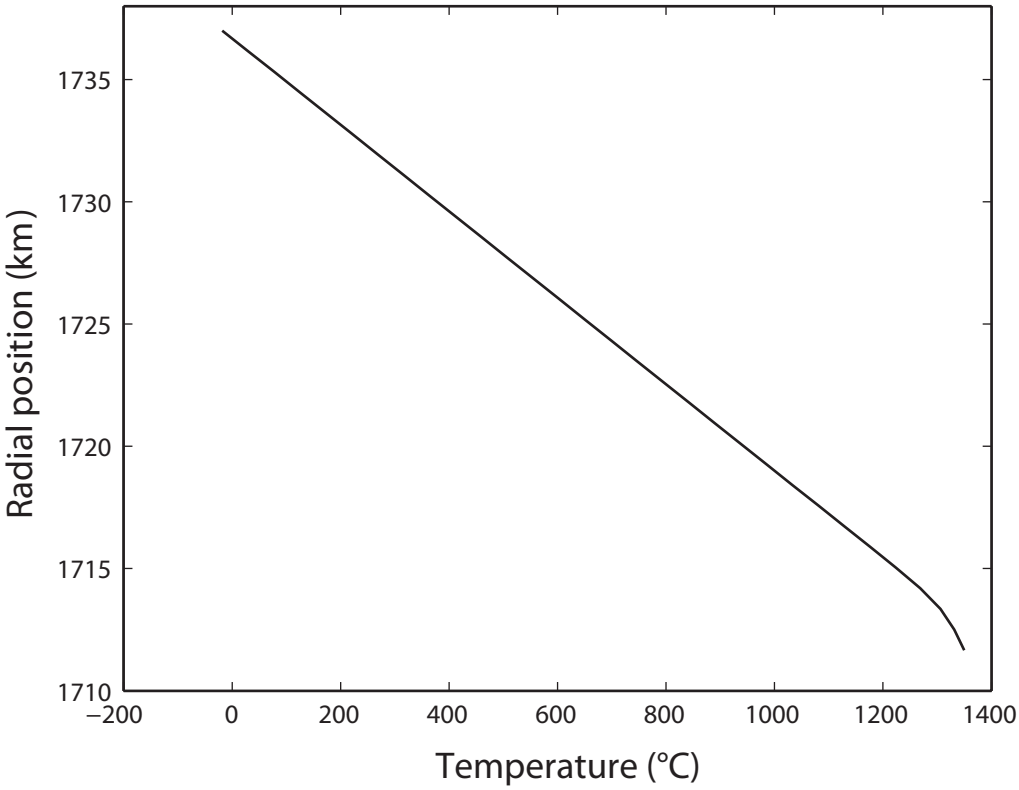

Figure S11. Crustal temperature profile for tidal heating model 38 (Table S13), for a point at (0° N, 0° E), where the surface temperature is -18.1°C and the local crustal thickness is 25.3 km. The basal temperature of 1350°C is not meant to represent a specific model of magma ocean cooling (see discussion in Section S8).

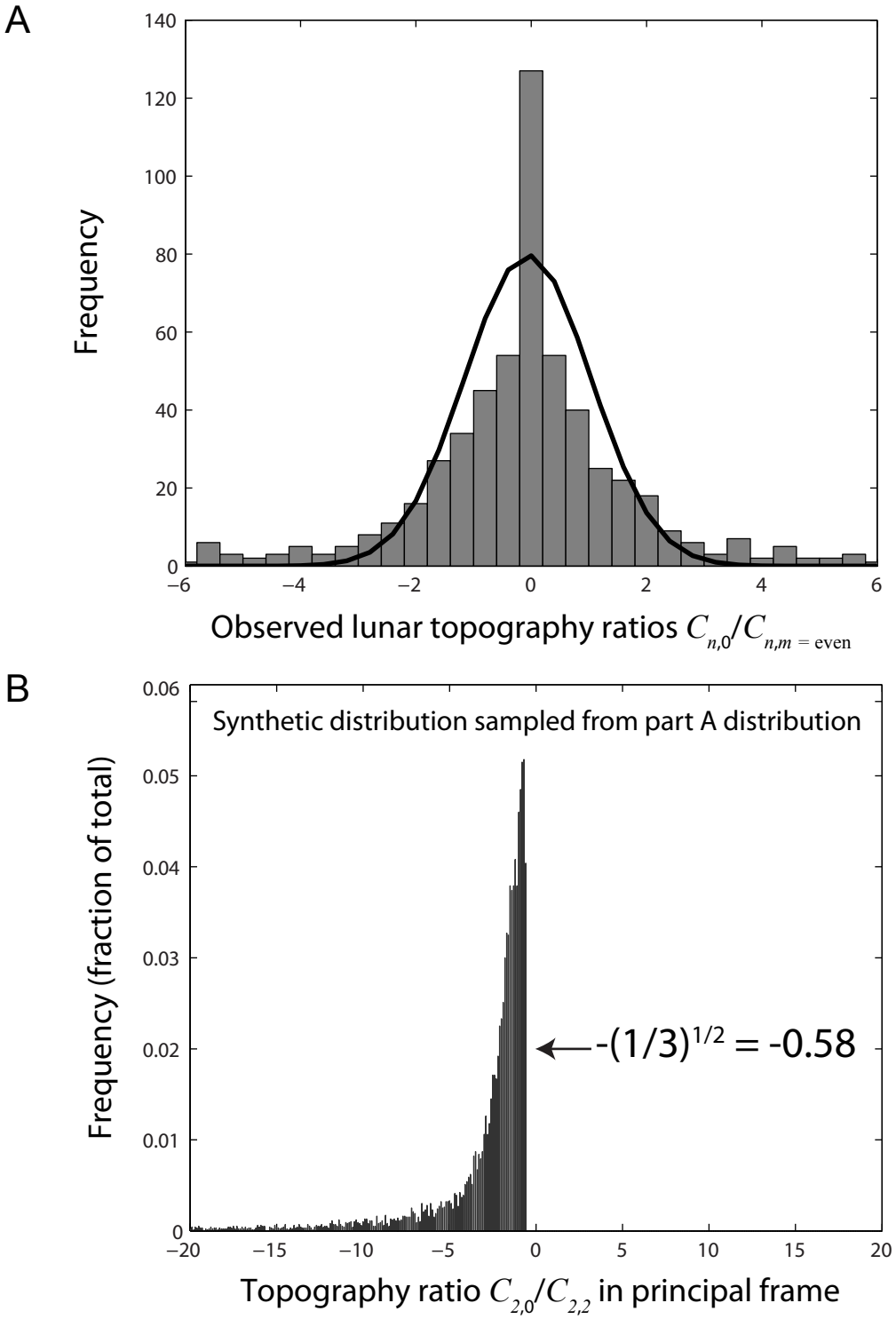

Figure S12. Distributions of coefficient ratios for lunar topography (Section S9). (**A**) Distribution of lunar topography coefficient ratios $C_{n,0}/C_{n,m}$ for even m, up to degree n = 50. The black line shows the best-fit Gaussian function. The ratios were truncated at -6 and +6 prior to fitting. (**B**) 10,000 ratio values taken from the best-fit distribution in part A and then rotated to the implied principal frame (taking those ratios to represent a ratio $C_{2,0}/C_{2,2}$), where the ratio was then recalculated and used to make the distribution shown (see text).

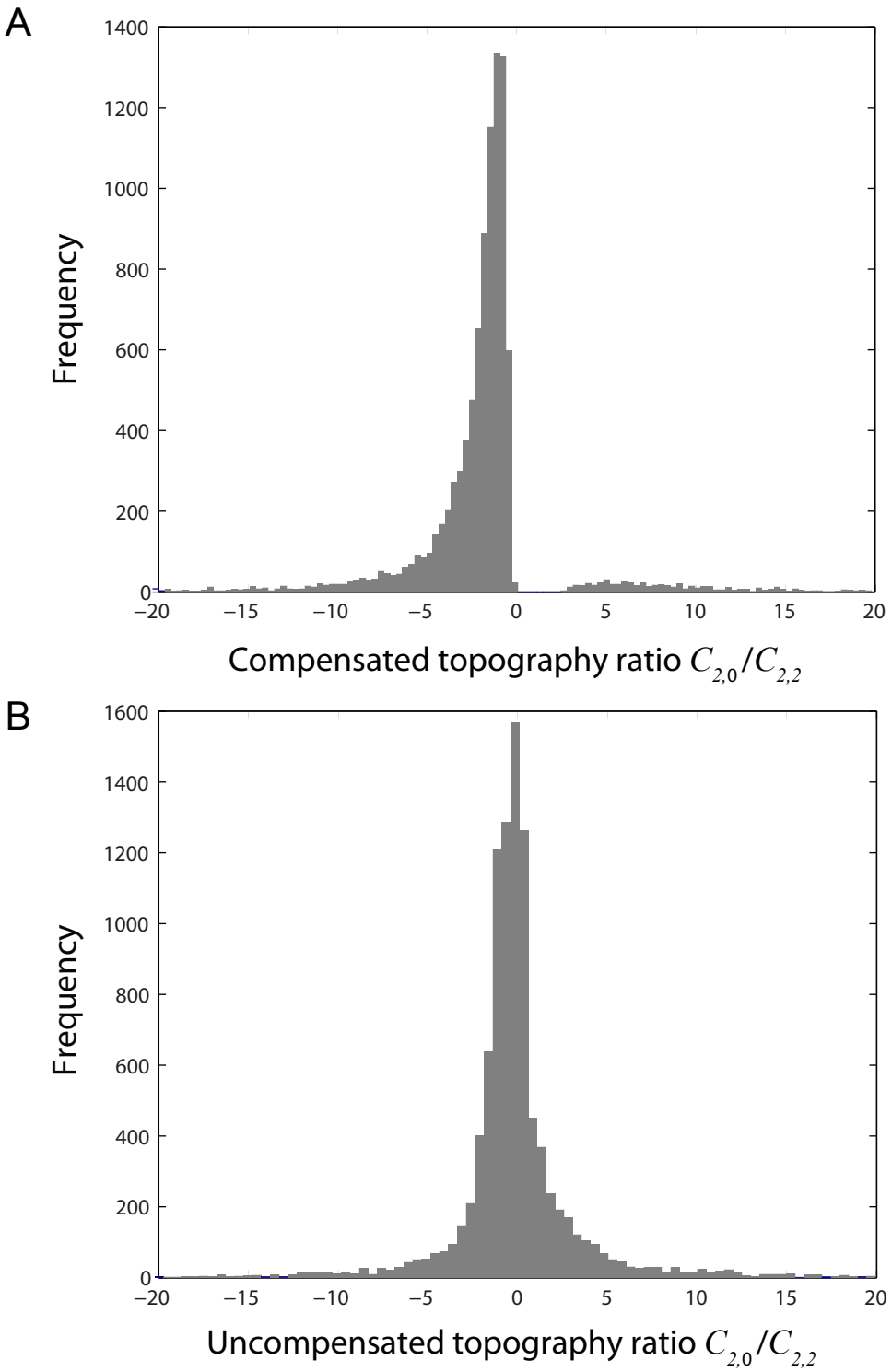

Figure S13. Distributions of $C_{2,0}/C_{2,2}$ coefficient ratios for compensated and uncompensated topography, derived from the lunar topography distribution in Fig. S12b, and a generated gravity component. (**A**) Compensated topography. (**B**) Uncompensated topography. The differences in each distribution come from weaker (compensated topography) and stronger (uncompensated topography) dependencies on gravity, which is partially generated from the input topography, and partially random.

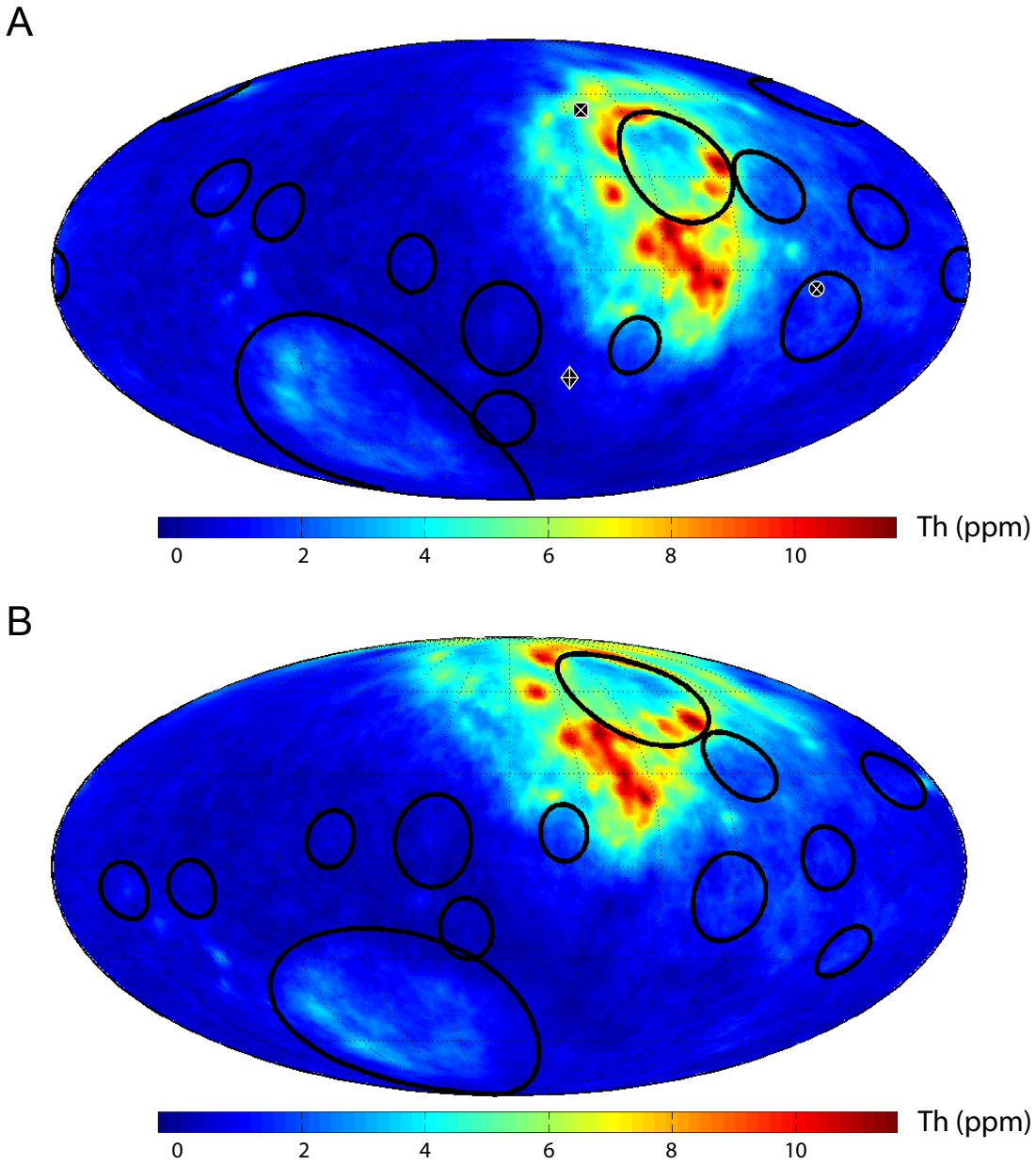

Figure S14. Lunar thorium distribution from Lunar Prospector data. (**A**) In the present reference frame. The black points show the primordial principal axes (compare with Figs. 2a-c). (**B**) In the basin-removed topography principal frame (compare with Figs. 2d-f).